

Dynamic Operation and Control of a Multi-Stack Alkaline Water Electrolysis System with Shared Gas Separators and Lye Circulation: A Model-Based Study

Yiwei Qiu^a, Jiatong Li^a, Yangjun Zeng^a, Yi Zhou^{a,*}, Shi Chen^a, Xiaoyan Qiu^a, Buxiang Zhou^a, Ge He^b, Xu Ji^b, Wenying Li^c

^aCollege of Electrical Engineering, Sichuan University, Chengdu, 610065, China

^bSchool of Chemical Engineering, Sichuan University, Chengdu, 610065, China

^cSichuan Tsinghua Energy Internet Research Institute, Chengdu, 610213, China

Abstract

An emerging approach for large-scale hydrogen production using renewable energy is to integrate multiple alkaline water electrolysis (AWE) stacks into a single balance of plant (BoP) system, sharing components such as gas-lye separation and lye circulation. This configuration, termed the N -in-1 AWE system, packs N stacks into a modular system, reducing land requirements, the complexity of plant topology, and overall capital costs. However, the coupling of these stacks through the shared BoP introduces challenges in dynamic operation under varying energy inputs, making their performance unclear compared to traditional 1-in-1 systems. To address this, we develop a state-space model of the N -in-1 AWE system, capturing the dynamic behaviors of lye circulation, temperature, and HTO impurity, and their impact on energy conversion efficiency. We then propose a nonlinear model predictive controller (NMPC) to coordinately optimize inter-stack electrolytic current distribution, lye flow, and cooling, enabling the system to dynamically track varying load commands while maximizing efficiency, stabilizing temperature, and limiting HTO impurity accumulation. Simulation studies on a 4,000 Nm³/h-rated 4-in-1 system verify the proposed controller under dynamic operation. Comparison with 4 independent 1-in-1 systems reveals that, with proper control, the N -in-1 configuration offers comparable flexibility in accommodating real-world wind power inputs. The average differences in the root-mean-square errors (RMSEs) for load-tracking and stack temperature stabilization, and specific energy consumption are below 0.014 MW, 2.356 K, and 0.003 kWh/Nm³.

Keywords: alkaline water electrolysis, nonlinear model predictive control, balance of plant (BoP), renewable power to hydrogen

*Corresponding author

Email address: yizhou3230@scu.edu.cn (Yi Zhou)

1. Introduction

1.1. Motivation

Water electrolysis for hydrogen production has emerged as a crucial pathway for renewable energy utilization and low-carbon energy transformation, with rapid scaling worldwide [1]. According to the IEA, the global installed capacity of hydrogen electrolyzers reached 1.4 GW in 2023, doubling from 2022 levels. Many countries have incorporated renewable power-to-hydrogen (ReP2H) into their strategic plans, targeting 520 GW of installed capacity by 2030 [2]. Among various hydrogen production technologies, alkaline water electrolysis (AWE) stands out for its maturity, large capacity, long lifespan, and low cost, making it a preferred choice in many ReP2H projects [3].

Although the capacity of a single AWE has increased from 1,000 Nm³/h (5 MW) in 2020 to 3,000 Nm³/h (15 MW) today [3], the scale remains relatively limited for large-scale applications. Due to the capacity constraints of a single electrolyzer, hydrogen plants often consist of dozens to hundreds of electrolyzers, leading to large land requirements, complex topologies, and high investment costs [3]. The acquisition and installation costs of electrolyzers, as well as land and infrastructure investments, are critical considerations in practices [4, 5]. To reduce costs and improve the economic viability of green hydrogen, shared balance-of-plant (BoP) designs have emerged as a technological route for scaling up AWE systems [4–11].

A typical AWE system consists of an electrolysis stack and a set of BoP system, which includes lye-gas separation, cooling, and lye circulation subsystems, and pumps, valves, instrumentation, and control systems, often integrated as a skid-mounted unit [3, 5]. This is referred to as a *1-in-1* system. However, in large hydrogen plants with many electrolyzers, adopting a 1-in-1 configuration results in excessive land use, complex topologies, and elevated costs. To address these issues, some projects employ *N-in-1* configurations (also referred to as *multi-electrolyzer* systems [12, 13],) wherein multiple stacks share a single BoP system, thereby reducing complexity and cost [5].

Engineering practice indicates that replacing a 1-in-1 configuration with a 2-in-1 system can reduce costs by 25% and land and utility requirements by 45%, while a 4-in-1 system can achieve savings of 35% and 55%, respectively [8]. Consequently, many large ReP2H projects adopt *N-in-1* configurations. For example, the *Baofeng Energy Green Hydrogen Development Project* and *Songwon Hydrogen Energy Industrial Park Project* utilize 2-in-1 systems as the basic production unit [14, 15], while the *Sinopec Kuqa Green Hydrogen Demonstration Project* and the *Da'an Wind and Solar Green Hydrogen Synthesis Ammonia Integration Demonstration Project* adopt 4-in-1 configurations to enable larger-scale plant designs [15, 16].

However, compared to 1-in-1 systems, *N-in-1* configurations introduce greater operational complexity due to coupling between stacks through the shared BoP system. This coupling affects temperature regulation and HTO impurity control, potentially limiting flexibility under varying power inputs [9]. Existing research on the dynamic operation of AWE systems, however, predominantly focuses on 1-in-1 systems, while studies

addressing N -in-1 configurations are limited; see Section 1.2 for literature review. Consequently, two key issues arise in engineering applications:

1. How do N -in-1 systems compare to 1-in-1 systems in terms of adaptability to variable power inputs, such as load flexibility and energy conversion efficiency? Does the capital cost saved in deploying N -in-1 systems come at the expense of operational flexibility?
2. How can controllers for N -in-1 AWE systems be designed to match the performance of 1-in-1 systems, minimizing potential losses in flexibility due to increased complexity?

To address these questions, this study develops a state-space model for N -in-1 AWE systems, designs controllers, and evaluates performance metrics. Given the lack of experimental platforms for laboratory-scale N -in-1 systems and the challenges of conducting experiments on industry-scale systems (20–40 MW or larger,) this study adopts a simulation approach. Section 1.2 summarizes the current research on AWE modeling and control, while Section 1.3 outlines the contributions of this study.

1.2. Literature Review

AWE has a long history of application. In recent years, the increasing practices of ReP2H projects have accelerated researches on AWE systems, yielding substantial results and insights.

Extensive studies have been conducted on the components of AWE systems. Many researches focus on the stacks, addressing topics such as electrochemical performance [17, 18], degradation [19], flow field [20], and the spatial distribution of temperature [21], bubbles [22], and stray currents [23–25]. Additional research has examined BoP components, including efficiency analysis and structural design of separators [26–28], heat exchangers [29, 30], pressure loss and energy consumption in lye circulation [23], and compression and purification networks [31].

Building on these component-level studies, researchers have developed complete AWE system models and designed controllers. For example, Ulleberg et al. [32] established a classic lumped dynamic model of electrochemical and thermal behavior. David et al. [33] developed a high-order mass transfer model that captures variations in pressure, liquid levels, and flow compositions. Qi et al. [34–36] proposed 1st- to 3rd-order state-space models to describe temperature dynamics and HTO impurity accumulation under dynamic loads, introducing thermal and pressure management methods to improve energy conversion efficiency and load range. Chen et al. [37] considered the impacts of temperature and pulse rectification on voltage and current efficiencies, proposing an adaptive MPPT strategy to optimize energy conversion efficiency across the full operating range. Li et al. [38] proposed a comprehensive control framework addressing temperature, pressure, and lye circulation to enhance performance over the full load range. These models have been validated through experiments at various scales (500 W to 3 MW) [39–41]. Qiu et al. [42] further developed

Table 1: Summary of the latest research related to process modeling and control of AWE systems

Literature	Configuration	Considered Processes					Controller
		Load control	Lye-gas separation	Lye circulation	Thermal control	HTO impurity	
Qi et al. 2023 [34, 35]	1-in-1	×	✓	✓	✓	×	MPC/PID
Qi et al. 2021 [36]	1-in-1	×	✓	✓	×	✓	MPC
Qiu et al. 2024 [46]	Multiple 1-in-1	✓	✓	✓	✓	✓	MPC
Cheng et al. 2024 [37]	1-in-1	✓	×	×	✓	×	MPPT
Li et al. 2022 [38]	1-in-1	✓	✓	✓	✓	✓	PID
Li et al. 2024 [47]	1-in-1	✓	✓	✓	✓	✓	MPC
Kang et al. 2018 [31]	Multiple 1-in-1	✓	×	×	×	×	Steady-state optimization
Rizwan et al. 2021 [9]	N -in-1 (Shared lye circulation)	✓	✓	✓	✓	×	Steady-state optimization
Chen et al. 2024 [10]	N -in-1 (Shared lye circulation)	✓	✓	✓	✓	✓	PSO-MPC
Shi et al. 2023 [11]	N -in-1 (Shared lye circulation)	✓	✓	✓	✓	×	DMC/MPC
Zheng et al. 2023 [48]	N -in-1 (Shared lye-gas separation and lye circulation)	✓	×	×	✓	×	PID/Rule-based
Liang et al. 2024 [12]	N -in-1 (Shared lye-gas separation and lye circulation)	✓	×	×	×	×	Rule-based
Li et al. 2023 [13]	N -in-1 (Shared lye-gas separation and lye circulation)	✓	×	✓	✓	×	Rule-based
This work	N -in-1 (Shared lye-gas separation and lye circulation)	✓	✓	✓	✓	✓	NMPC

an online identification method for heat and mass transfer parameters, enabling real-time model calibration and health diagnostics. A comprehensive review of AWE modeling and control is provided in [43–45].

In contrast to extensive researches on the 1-in-1 configuration, only a few studies have focused on the N -in-1 configuration. Among these, systems sharing only lye circulation (referred to as *weakly coupled* systems [10]) have been more explored than those sharing both separation and lye circulation subsystems (referred to as *strongly coupled* systems [10].)

For the weakly coupled configurations, Rizwan et al. [9] investigated thermal management, and proposed a capacity optimization method based on the steady-state model. Chen et al. [10] introduced a model predictive controller (MPC) that integrates thermal, lye flow, and pressure control. Shi et al. [11] proposed an RTO-PID dual-layer temperature controller. However, the weakly coupled systems studied in [9–11] have relatively fewer applications. Many N -in-1 systems in large-scale projects [14–16] adopt strongly coupled topologies, which offer further cost reductions but increase control complexity.

For strongly coupled systems, Zheng et al. [48] analyzed inter-stack load distribution in a 4-in-1 system driven by off-grid wind turbines, but the rule-based controller employed cannot ensure optimality. Studies

such as [12, 13, 49] considered startup and shutdown scheduling for N -in-1 systems, proposing rule-based strategies with the on-off states of the stacks in one system bonded. However, these studies neglected dynamic temperature behavior within AWE systems. Furthermore, none of the above works addressed HTO impurity, which is critical in dynamic operation, especially at low loads.

Research on the model and control of AWE systems is summarized in Table 1. It highlights that existing studies on N -in-1 systems remain insufficient. Despite the widespread adoption of N -in-1 designs in practices (see Section 1.1), studies on production scheduling [50–52], energy management [53, 54], and power system ancillary services [55, 56] in hydrogen plants are predominantly based on the 1-in-1 configuration. However, the applicability of these studies to N -in-1 systems remains unclear, leaving the two questions raised in Section 1.1 to answer.

1.3. Contributions of This Work

To address the research gap identified in Section 1.2, this study conducts an exploratory study of N -in-1 AWE systems with stacks sharing both gas separators and the lye circulation loop, aiming to answer the questions raised in Section 1.1. The main contributions are as follows:

1. A state-space model is developed for N -in-1 AWE systems, accounting for shared lye-gas separation and lye circulation and their impact on the behaviors of energy conversion efficiency, thermal dynamics, and HTO impurity accumulation.
2. A nonlinear model predictive controller (NMPC) is proposed for N -in-1 AWE systems, addressing challenges posed by the coupling among multiple stacks and the BoP system, to achieve optimal control under varying energy inputs.
3. Comparative simulations reveal the similarities and differences between N -in-1 and 1-in-1 systems in terms of efficiency, flexibility, and other performance metrics.

The structure of this paper is as follows: Section 2 describes the flowsheets of the N -in-1 AWE system; Section 3 establishes the state-space model of the N -in-1 system; Section 4 introduces the controller design for dynamic operation; Simulation studies are carried out in Section 5; finally, Section 6 concludes with findings and future perspectives.

2. Flowsheets Description

2.1. System Topology

Fig. 1 illustrates the typical flowsheets of an N -in-1 AWE system. The hydrogen-lye and oxygen-lye mixtures from the stacks are mixed and routed to separators. After separation, the gaseous hydrogen and oxygen are discharged. System pressure and the liquid levels on both sides are regulated via gas outlet valves [33]. The separated lye is cooled via heat exchangers. Afterward, desalinated water is replenished

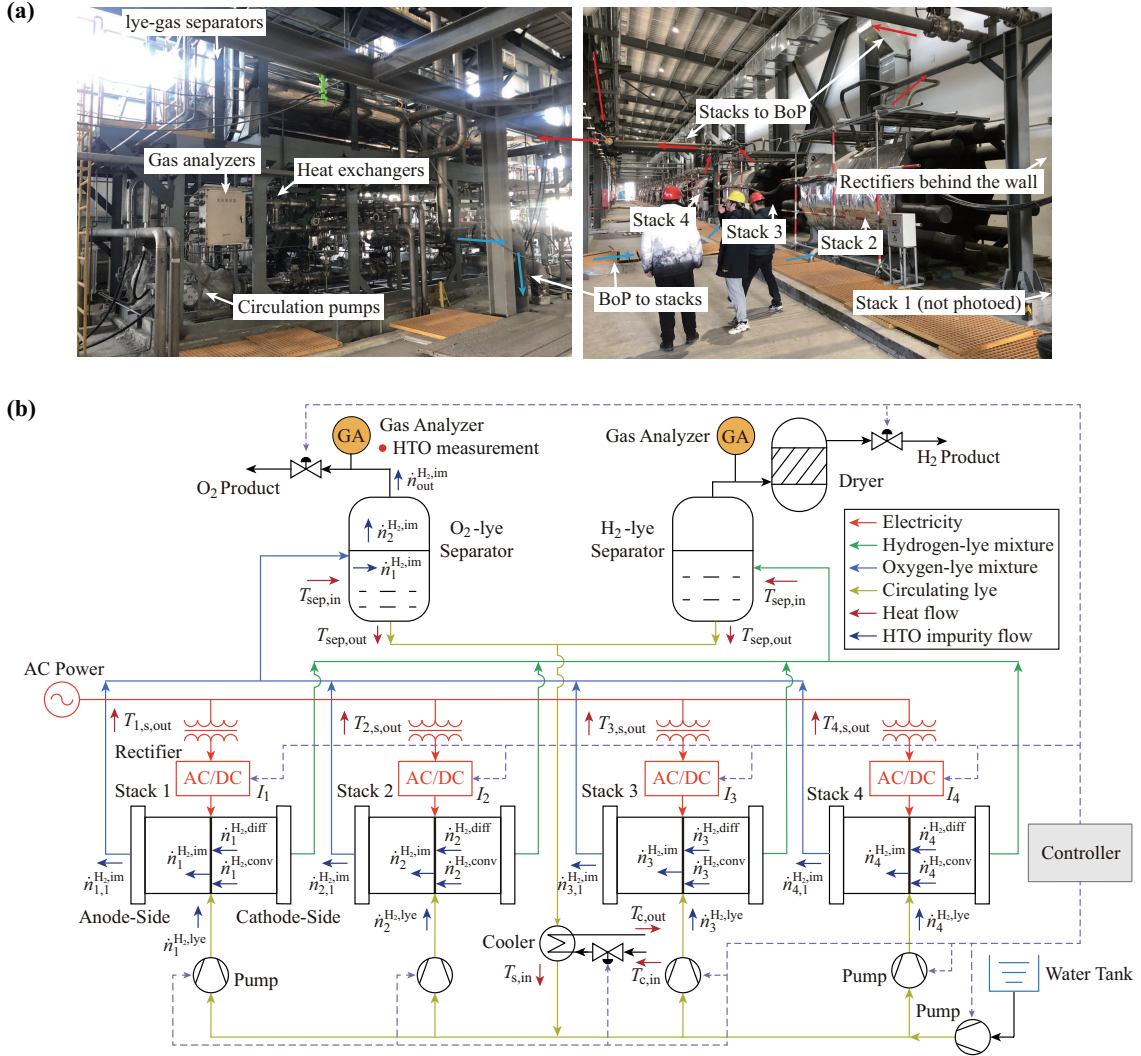


Figure 1: (a) Photo of 4-in-1 AWE systems in installation. (b) Schematic diagram of a typical 4-in-1 AWE system.

into the lye before it is redistributed to the stacks by circulation pumps. Detailed topologies vary among manufacturers and are further discussed in Section 3.2.1.

On the electrical side, each stack is connected to a rectifier for dc power supply, allowing independent adjustment of load power. In some cases, a multi-winding transformer with phase-shift secondary windings replaces multiple transformers to reduce costs and minimize harmonic injections [53, 57]. Note that some literature discusses multiple stacks sharing a single rectifier; however, due to challenges such as current equalization, insulation, and reduced flexibility, this configuration is not a common application.

The stacks are interconnected through the BoP, and their energy conversion efficiency, temperature, and HTO impurity accumulation under varying power inputs are directly influenced by controls on stack power, lye flow, and cooling. To capture the complex relation between control and responses, this paper develops

a state-space model of the N -in-1 system in Section 3 to support controller design.

2.2. Assumptions

To simplify the model without loss of generality, the following assumptions are made:

a) Pressure Dynamics: While pressure affects energy conversion efficiency [32], and lowering the pressure can alleviate HTO accumulation to expand the load range [36], adjusting pressure may induce structural fatigue and reduce lifespan. Consequently, pressure adjustment is rarely employed in practice. In addition, pressure and liquid levels in separators are typically stabilized by independent PID controllers, which are effectively decoupled from efficiency, temperature, and HTO accumulation dynamics. Following related studies [12, 13, 36], this work assumes the AWE system operates at a fixed pressure of 1.6 MPa.

b) Inter-Stack Stray Current: Due to the pipeline between stacks being much longer compared to the channels in the stacks, stray currents are predominantly confined to the interior of the stacks [25]. Thus, inter-stack stray currents are neglected.

c) Water Consumption and Replenishment: The processes of water consumption and replenishment are much slower than the variations in current, temperature, and HTO impurity crossover, and these processes have minimal impact on control performance. Hence, they are neglected in this work.

d) Symmetry Between Stacks and BoP Components: Many industrial AWE systems feature symmetric geometry design for cathode- and anode-side flowsheets. For simplicity, we assume thermal models are identical for both sides. Moreover, we assume the geometric parameters of the N stacks are the same.

3. State-Space Models of the N -in-1 AWE System

Compared to the 1-in-1 system, the dynamic behavior of the N -in-1 system is more complex due to the coupling of heat and mass flows between stacks. Based on the classical literature [32] and the authors' prior research on 1-in-1 systems [34–36], we establish a state-space model for the N -in-1 system. Here, we will pay more attention to the unique aspects of the N -in-1 system while briefly introducing the components that also appear in 1-in-1 systems for completeness. The key variables are marked in Fig. 1(b).

3.1. Electrochemical and Production Models

This process of converting electricity to hydrogen is described using the production model. First, the cell voltage of each stack ($i = 1, \dots, N$) is modeled using the semi-empirical equations [17]:

$$U_i^{\text{cell}} = U_i^{\text{rev}} + (r_{i,1} + r_{i,2}T_{i,s} + r_{i,3}\rho) I_i + s_i \log \left[\left(t_{i,1} + \frac{t_{i,2}}{T_{i,s}^2} + \frac{t_{i,3}}{T_{i,s}^2} \right) I_i + 1 \right], \quad (1)$$

where U_i^{cell} , I_i , and $T_{s,i}$ are the cell voltage, current, and stack temperature; $U_i^{\text{rev}} = 1.23$ V is the reversible voltage; ρ is the pressure; $r_{i,1}$, $r_{i,2}$, $r_{i,3}$, s_i , $t_{i,1}$, $t_{i,2}$ and $t_{i,3}$ are constant parameters.

Due to the existence of stray currents, not all current contributes to hydrogen production; some flows through the channels and dissipates. The current efficiency, known as *Faraday efficiency*, is modeled by:

$$\eta_i^{\text{cell}} = \frac{(0.1I_i)^2}{f_{i,1} + (0.1I_i)^2} f_{i,2}, \quad (2)$$

where $f_{i,1}$ and $f_{i,2}$ are coefficients related to temperature and pressure.

The hydrogen and oxygen production rates and power consumption of each stack are calculated as:

$$\dot{n}_i^{\text{H}_2, \text{prod}} = \eta_i^{\text{cell}} N^{\text{cell}} I_i / (2F), \quad (3)$$

$$\dot{n}_i^{\text{O}_2, \text{prod}} = \eta_i^{\text{cell}} N^{\text{cell}} I_i / (4F), \quad (4)$$

$$P_i^{\text{ele}} = N^{\text{cell}} U_i^{\text{cell}} I_i, \quad (5)$$

where $F = 96,485 \text{ C/mol}$ is the Faraday's constant; N^{cell} is the number of cells in a stack.

Note that the energy conversion efficiency depends on stack temperature, showing a nonlinear coupling with the heat and mass transfer processes discussed in Section 3.2.2. This poses challenges for controller design. We later addressed them in Section 4.4. Moreover, the parameters may vary due to degradation and can be calibrated via an online estimator developed in our prior study [42]. The electrochemical model of individual stacks is the same as that of the 1-in-1 system and will not be elaborated.

3.2. Lye Circulation, Heat Transfer and HTO Impurity Accumulation Models

3.2.1. Lye Circulation and Inter-Stack Distribution

Typical lye circulation topologies for commercial N -in-1 systems are shown in Fig. 2. Some systems employ an independent pump for each stack, as shown in Fig. 2(a), allowing independent lye flow control. Other designs, such as Figs. 2(b) and 2(c), share pumps among multiple stacks. In these cases, lye flow distribution depends on the load of the stacks. Using Fig. 2(c) as an example, the lye flow distribution model is derived as follows.

The flow rate of lye-gas mixture in each stack satisfies Poiseuille's law [33]:

$$\Delta p_i = v_{i, \text{mix}}^{\text{ca/an}} R_i^{\text{ca/an}}, \quad (6)$$

where Δp_i is the pressure drop across the i th stack; $v_{i, \text{lye}}^{\text{ca/an}}$ is the flow rate of cathode/node-side lye-gas mixture; and $R_i^{\text{ca/an}}$ is the flow resistance.

As stacks are connected at both ends, as shown in Fig. 1(b), their pressure drops are identical. Therefore, the flow rates are inversely proportional to flow resistance:

$$\frac{v_{i, \text{mix}}^{\text{ca/an}}}{v_{j, \text{mix}}^{\text{ca/an}}} = \frac{R_j^{\text{ca/an}}}{R_i^{\text{ca/an}}}. \quad (7)$$

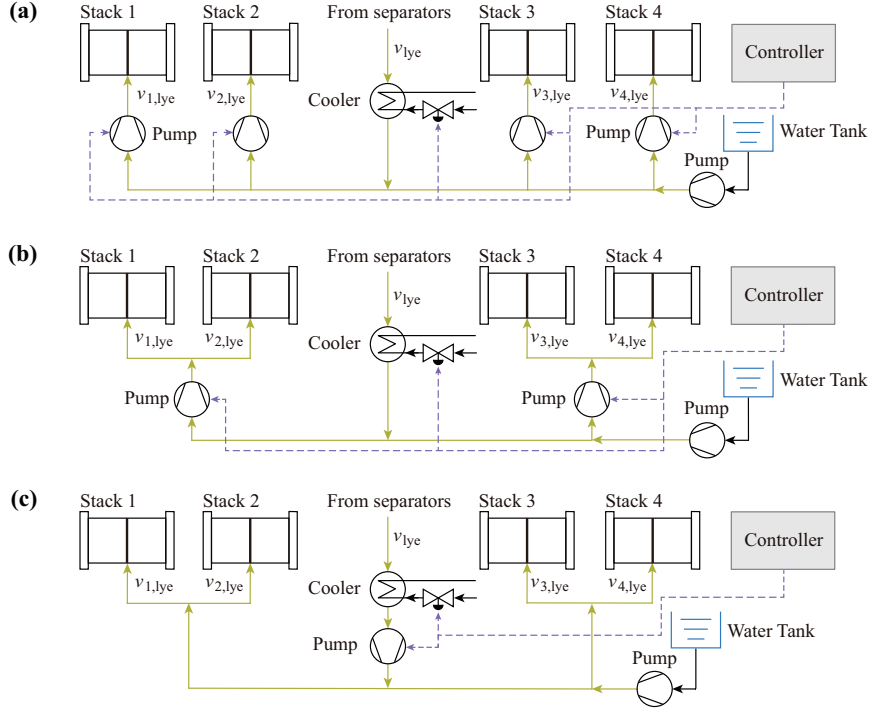


Figure 2: Topologies for inter-stack lye flow distribution. (a) 4 lye circulation pumps. (b) 2 lye circulation pumps. (c) 1 lye circulation pump.

Under laminar flow assumptions, $R_i^{\text{ca/an}}$ can be approximated as:

$$R_i^{\text{ca/an}} = \frac{128\mu_{j,\text{mix}}^{\text{ca/an}}l}{\pi d^4}, \quad (8)$$

where l and d are the equivalent length and diameter of the flow paths; and $\mu_{j,\text{mix}}^{\text{ca/an}}$ is the dynamic viscosity of the lye-gas mixture, which can be approximated as a volume-weighted average of the dynamic viscosities of the lye μ_{lye} and the gas $\mu_{\text{H}_2/\text{O}_2}$ [33]:

$$\mu_{i,\text{mix}}^{\text{ca/an}} = \frac{V_{i,\text{gas}}^{\text{ca/an}} \mu_{\text{H}_2/\text{O}_2} + V_{i,\text{lye}}^{\text{ca/an}} \mu_{\text{lye}}}{V_{i,\text{gas}}^{\text{ca/an}} + V_{i,\text{lye}}^{\text{ca/an}}} = \alpha_i^{\text{ca/an}} \mu_{\text{H}_2/\text{O}_2} + (1 - \alpha_i^{\text{ca/an}}) \mu_{\text{lye}}, \quad (9)$$

where $V_{i,\text{lye}}^{\text{ca/an}}$ and $V_{i,\text{gas}}^{\text{ca/an}}$ are the volumes of the lye and gas in the i th stack; $\alpha_i^{\text{ca/an}}$ represents the volumetric gas ratio, calculated as:

$$\alpha_i^{\text{ca/an}} = \frac{V_{i,\text{gas}}^{\text{ca/an}}}{V_{i,\text{gas}}^{\text{ca/an}} + V_{i,\text{lye}}^{\text{ca/an}}} = \frac{\dot{n}_i^{\text{H}_2/\text{O}_2,\text{prod}} RT_{s,i}}{\rho v_{i,\text{mix}}^{\text{ca/an}}}, \quad (10)$$

where R is the gas constant.

The flow rates of gas and lye $v_{i,\text{gas}}^{\text{ca/an}}$ and $v_{i,\text{lye}}^{\text{ca/an}}$ can be then extracted as:

$$\begin{cases} v_{i,\text{gas}}^{\text{ca/an}} = \alpha_i^{\text{ca/an}} v_{i,\text{mix}}^{\text{ca/an}}, \\ v_{i,\text{lye}}^{\text{ca/an}} = (1 - \alpha_i^{\text{ca/an}}) v_{i,\text{mix}}^{\text{ca/an}}, \end{cases} \quad (11a) \quad (11b)$$

which are later used for the thermal and HTO impurity models in Sections 3.2.2 and 3.2.3.

From the above discussion, we know that the gas ratio is related to gas production. Different electrolytic power leads to varying gas ratios, affecting flow resistances and consequently the inter-stack lye flow distribution. Compared with the 4-pump topology in Fig. 2(a), the 1-pump topology in Fig. 2(c) has less flexibility in regulating lye flow. Nevertheless, with appropriate control, the system's performance will not be adversely affected, as detailed in Section 5.4.

Remark 1. *Considering that the viscosity of gases (around 0.9×10^{-5} Pa·s for hydrogen and 2.2×10^{-5} Pa·s for oxygen) is orders of magnitude lower than that of lye (around 2.3×10^{-3} Pa·s), i.e., $\mu_{\text{H}_2/\text{O}_2} \ll \mu_{\text{lye}}$, the former can be neglected in (9), yielding $\mu_{i,\text{mix}}^{\text{ca/an}} \approx (1 - \alpha_i^{\text{ca/an}})\mu_{\text{lye}}$. Further, by comparing (11a) and (11b), it follows that for different i and j , we have $v_{i,\text{lye}}^{\text{ca/an}} \approx v_{j,\text{lye}}^{\text{ca/an}}$, meaning that even if the operating points of the stacks differ, the liquid-phase flow can be considered to distribute evenly. Moreover, the lye flow rates on the cathode and anode sides can be assumed equal, i.e., $v_{i,\text{lye}}^{\text{ca}} \approx v_{i,\text{lye}}^{\text{an}}$. We further denote $v_{i,\text{lye}} = v_{i,\text{lye}}^{\text{ca}} + v_{i,\text{lye}}^{\text{an}}$.*

3.2.2. Heat Transfer

Temperature affects the efficiency, safety, and flexibility of the AWE systems. As shown in Section 3.1, low temperature increases overvoltage, reducing energy conversion efficiency, while excessively high temperature imposes excessive thermal stress, shortening the lifespan of electrodes, diaphragm, and sealing materials. For the 1-in-1 AWE system, our previous studies [34] proposed a 3rd-order state-space model to capture the heat transfer behaviors among the stack, separators, and heat exchanger. In this work, we further extend this model to N -in-1 AWE systems.

In an N -in-1 system, the temperature of each stack and its internal lye flow is jointly determined by electrolytic heat, lye-gas flow, and heat dissipation to the environment, modeled as:

$$C_{i,s} \frac{dT_{i,s,\text{out}}}{dt} = Q_{i,\text{ele}} - Q_{i,s,\text{diss}} - c_{\text{lye}} v_{i,\text{lye}} \rho_{\text{lye}} (T_{i,s,\text{out}} - T_{i,s,\text{in}}), \quad (12)$$

where $C_{i,s}$ denotes the total heat capacity of the stack and the lye inside it, i.e., $C_{i,s} = C_{i,\text{struc},s} + C_{i,\text{lye},s}$, with $C_{i,\text{lye},s} = V_{i,s,\text{lye}} \rho_{\text{lye}} c_{\text{lye}}$; $V_{i,s,\text{lye}}$ is the volume of the lye in the stack; $\rho_{\text{lye}} = 1,250$ kg/m³ and $c_{\text{lye}} = 3,300$ J/(kg·K) are the density and specific heat capacity of the lye; $T_{i,s,\text{in}}/T_{i,s,\text{out}}$ denotes the inlet/outlet lye temperature the i th stack; $Q_{i,\text{ele}}$ denotes heating flow; $Q_{i,\text{diss},s}$ denotes heat dissipation to the environment.

Note that, as indicated in Fig. 1(b), the inlet temperature of the stacks is the same, while the outlet temperature varies due to differences in the temperature and load among stacks.

The heating flow $Q_{i,\text{ele}}$ comprises the heat released by the electrolytic reaction and the ohmic heat from the stray current, as:

$$Q_{i,\text{ele}} = \eta_i^{\text{cell}} N^{\text{cell}} I_i (U_i^{\text{cell}} - U^{\text{th}}) + (1 - \eta_i^{\text{cell}}) N^{\text{cell}} I_i U_i^{\text{cell}}, \quad (13)$$

where $U^{\text{th}} = 1.48$ V is the thermoneutral voltage.

Heat dissipation $Q_{i,s,\text{diss}}$ from the i th stack to the environment includes convection and radiation, denoted as $Q_{i,s,\text{conv}}$ and $Q_{i,s,\text{rad}}$, which follow:

$$Q_{i,s,\text{diss}} = Q_{i,s,\text{conv}} + Q_{i,s,\text{rad}} = h_s A_{s,\text{diss}} (T_{i,s,\text{out}} - T_{\text{am}}) + \sigma A_{s,\text{diss}} \epsilon_s (T_{i,s,\text{out}}^4 - T_{\text{am}}^4), \quad (14)$$

where $A_{s,\text{diss}}$ is the heat dissipation area; T_{am} is the ambient temperature; σ is the Stefan-Boltzmann constant; ϵ_s denotes the emissivity of the stack; and h_s is the natural convection coefficient, following [58]:

$$h_s = 2.51 \times 0.52 [(T_{i,s,\text{out}} - T_{\text{am}}) / \phi_s]^{0.25}, \quad (15)$$

where ϕ_s represents the diameter of the stack.

As indicated in Fig. 1, the lye exiting the N stacks is mixed before entering the separators. Assuming no heat loss in pipes, the separator inlet temperature $T_{\text{sep,in}}$ is the weighted average of the outlet lye temperatures of the N stacks:

$$T_{\text{sep,in}} = \frac{\sum_{i=1}^N v_{i,\text{lye}} T_{i,s,\text{out}}}{v_{\text{tot,lye}}}, \quad (16)$$

where $v_{\text{tot,lye}} = \sum_{i=1}^N v_{i,\text{lye}}$ denotes total lye flow.

For the separators, assuming the heat carried by gaseous hydrogen/oxygen is negligible, the temperature is determined by

$$C_{\text{sep}} \frac{dT_{\text{sep,out}}}{dt} = \frac{1}{2} c_{\text{lye}} v_{\text{tot,lye}} \rho_{\text{lye}} (T_{\text{sep,in}} - T_{\text{sep,out}}) - Q_{\text{sep,conv}} - Q_{\text{sep,rad}}, \quad (17)$$

where C_{sep} is the heat capacity of the separator and lye inside it; $T_{i,\text{sep,out}}$ is the separator outlet temperature; $Q_{\text{sep,conv}}$ and $Q_{\text{sep,rad}}$ are the convective and radiative dissipation, calculated similarly to (14)–(15).

The lye left the cathode and anode-side separators is mixed and cooled before being circulated to the stack. Assuming the heat exchanger is a commonly used counterflow type, we have

$$C_{\text{he}} \frac{dT_{s,\text{in}}}{dt} = c_{\text{lye}} v_{\text{tot,lye}} \rho_{\text{lye}} (T_{\text{sep,out}} - T_{s,\text{in}}) - k A_c \Delta T, \quad (18)$$

where C_{he} is the total heat capacity of the heat exchanger and lye it contains; A_c represents heat exchange area; k is the heat transfer coefficient; and ΔT is the logarithmic temperature difference, as:

$$\Delta T = \frac{(T_{s,\text{in}} - T_{c,\text{out}}) - (T_{\text{sep,out}} - T_{c,\text{in}})}{\log [(T_{s,\text{in}} - T_{c,\text{out}}) / (T_{\text{sep,out}} - T_{c,\text{in}})]}, \quad (19)$$

where $T_{c,\text{in}}$ denotes the inlet cooling water temperature, which is regulated by a chiller and we assume it to be constant; $T_{c,\text{out}}$ denotes the outlet temperature of cooling water, determined as follows:

$$C_c \frac{dT_{c,\text{out}}}{dt} = c_c v_c \rho_c (T_{c,\text{in}} - T_{c,\text{out}}) + k A_c \Delta T, \quad (20)$$

where C_c denotes the total heat capacity of the cooling coil and the cooling water it contains; $c_c = 4,100$ J/(kg·K) and $\rho_c = 1,000$ kg/m³ are the specific heat capacity and density of the cooling water, respectively; and v_c represents the cooling water flow rate, which is regulated by a valve.

For an N -in-1 system, the heat transfer model (12)–(20) has an order of $N + 3$. This model links temperature dynamics with control of electrolytic load, lye flow, and cooling water. The temperatures also appear in the electrochemical model in Section 3.1 and the HTO impurity accumulation model in Section 3.2.3, showing coupling relations, which is addressed in the controller design in Section 4.

3.2.3. HTO Impurity Accumulation

Gas crossover between the anode and cathode sides occurs due to the non-compactness of the diaphragm and the mixing of lye returned from the hydrogen-side and oxygen-side separators. Once the HTO impurity concentration reaches half the flammability limit (2 vol%), the safety system shuts down the electrolyzer to prevent explosions [17]. Since HTO impurity accumulation impacts the lower load limit, it must be accounted for in controller design. Here, we extend the 3rd-order model for 1-in-1 systems proposed in our previous work [36] to the N -in-1 system.

In each stack of the N -in-1 system, the HTO impurity crossovers from the cathode-side half-cell to the anode-side half-cell via lye circulation [33], diffusion [59], and convection [59]:

$$\dot{n}_i^{\text{H}_2, \text{im}} = \dot{n}_i^{\text{H}_2, \text{lye}} + \dot{n}_i^{\text{H}_2, \text{diff}} + \dot{n}_i^{\text{H}_2, \text{conv}}, \quad (21)$$

where $n_{\text{lye}}^{\text{H}_2}$, $n_{\text{lye}}^{\text{H}_2}$, and $n_{\text{conv}}^{\text{H}_2}$ are the molar flows of HTO impurity brought in by lye circulation, diffusion, and convection, respectively.

As shown in Fig. 1, the circulating lye contains dissolved hydrogen due to the mixing of the return flows from hydrogen-side and oxygen-side separators. The corresponding molar flow of HTO impurity, $\dot{n}_i^{\text{H}_2, \text{lye}}$, depends on the distribution of lye flow across the N stacks (see Section 3.2.1), following [33]:

$$\dot{n}_i^{\text{H}_2, \text{lye}} = S^{\text{H}_2} \rho v_{i, \text{lye}} / 4, \quad (22)$$

where S^{H_2} is the solubility of hydrogen in the lye.

The crossover molar flows of HTO impurities due to diffusion and convection, $\dot{n}_i^{\text{H}_2, \text{diff}}$ and $\dot{n}_i^{\text{H}_2, \text{conv}}$, are determined by Fick's law and Darcy's law [59], respectively, as:

$$\begin{cases} \dot{n}_i^{\text{H}_2, \text{diff}} = A^{\text{cell}} N^{\text{cell}} \frac{D_{\text{eff}}^{\text{H}_2} \Delta c^{\text{H}_2}}{\delta} \approx A^{\text{cell}} N^{\text{cell}} \frac{D_{\text{eff}}^{\text{H}_2} S^{\text{H}_2} \rho}{\delta}, & (23\text{a}) \\ \dot{n}_i^{\text{H}_2, \text{conv}} = A^{\text{cell}} N^{\text{cell}} \frac{K_{\text{eff}}^{\text{H}_2}}{\mu_{i, \text{lye}}} S^{\text{H}_2} \rho \frac{\Delta \rho}{\delta}, & (23\text{b}) \end{cases}$$

where $D_{\text{eff}}^{\text{H}_2}$ is the diffusion coefficient; Δc^{H_2} denotes the differential concentration of hydrogen between the cathode and anode sides; δ is the thickness of the diaphragm; $K_{\text{eff}}^{\text{H}_2}$ is the permeability of the hydrogen through the diaphragm; $\Delta \rho$ denote the pressure difference between two sides, usually caused by fluctuations in pressure and liquid levels.

The HTO impurity is transported and accumulates throughout the system in three stages, including the anode half-cell, the liquid phase of the separator, and the gas phase of the separator, as shown in Fig. 1.

Based on molar volume conservation, we establish a state-space model for HTO accumulation in the N -in-1 system, similar to our prior work [36], as:

$$\begin{cases} \frac{dn_i^{\text{H}_2,\text{an}}}{dt} = \dot{n}_i^{\text{H}_2,\text{im}} - \dot{n}_{i,1}^{\text{H}_2,\text{im}}, & i = 1, \dots, N, \end{cases} \quad (24a)$$

$$\begin{cases} \frac{dn_{\text{liq}}^{\text{H}_2,\text{sep}}}{dt} = \sum_{i=1}^N \dot{n}_{i,1}^{\text{H}_2,\text{im}} - \dot{n}_2^{\text{H}_2,\text{im}}, \end{cases} \quad (24b)$$

$$\begin{cases} \frac{dn_{\text{gas}}^{\text{H}_2,\text{sep}}}{dt} = \dot{n}_2^{\text{H}_2,\text{im}} - \dot{n}_{\text{out}}^{\text{H}_2,\text{im}}, \end{cases} \quad (24c)$$

where $n_i^{\text{H}_2,\text{an}}$, $n_{\text{liq}}^{\text{H}_2,\text{sep}}$, and $dn_{\text{gas}}^{\text{H}_2,\text{sep}}$ represent the molar quantities of HTO impurity in the anode half-cell of the i th stack, and the liquid and gas phases of the separator, respectively; $\dot{n}_{i,1}^{\text{H}_2,\text{im}}$, $\dot{n}_2^{\text{H}_2,\text{im}}$, and $\dot{n}_{\text{out}}^{\text{H}_2,\text{im}}$ are the molar flows of HTO impurity, which satisfies:

$$\begin{cases} \dot{n}_{i,1}^{\text{H}_2} = \frac{n^{\text{H}_2,\text{an}} v_{i,\text{lye}}}{2V_{\text{lye}}^{\text{an}}}, & i = 1, \dots, N, \end{cases} \quad (25a)$$

$$\begin{cases} \dot{n}_2^{\text{H}_2} = \frac{N n_{\text{liq}}^{\text{H}_2,\text{sep}}}{\tau_{\text{sep}}}, \end{cases} \quad (25b)$$

$$\begin{cases} \dot{n}_{\text{out}}^{\text{H}_2} = \frac{RT_{\text{sep},\text{out}} N_{\text{gas}}^{\text{H}_2,\text{sep}} \sum_{i=1}^N n_i^{\text{O}_2,\text{prod}}}{\rho V_{\text{sep},\text{gas}}}, \end{cases} \quad (25c)$$

where $V_{\text{an}}^{\text{lye}}$ is the volume of lye in the anode-side half-cell; τ_{sep} is the separation time constant; $V_{\text{sep},\text{gas}}$ is the gas-phase volume of the separator.

The HTO impurity concentration in the gas phase of the oxygen-side separator, which is measured and taken as the safety metric [33, 36, 59], follows:

$$\text{HTO} = \frac{n_{\text{gas}}^{\text{H}_2,\text{sep}} RT_{\text{sep},\text{out}}}{\rho V_{\text{sep},\text{gas}}}. \quad (26)$$

Compared to the 1-in-1 system model in [36], the model order of the N -in-1 system increases to $N+2$. The accumulation process depends not only on the overall power but also on inter-stack load allocation and lye flow control, significantly increasing the complexity. The HTO impurity accumulation process is also integrated into the controller to accommodate the varying energy input; see Section 4 for details.

3.3. Model Summary

Summarizing the submodels established in Sections 3.1 and 3.2, Table 2 presents an overview of the state-space model for the N -in-1 AWE system. Note that the electrochemical and inter-stack lye distribution submodels are formulated by algebraic equations. Their state spaces are zero in dimension. Consequently, the complete state-space model has an order of $2N + 5$.

For easy understanding, Fig. 3 provides an illustration of the interrelationships among control and responses. We can observe that processes of hydrogen production, thermal dynamics, and HTO impurity accumulation are mutually coupled; see examples in Section 5.2. Furthermore, compared to the 1-in-1

Table 2: Summary of the proposed state-space model of the N -in-1 AWE system

Submodel	Electrochemical and production	Lye flow distribution	Heat transfer	HTO impurity accumulation
State variables	/	/	$T_{s,in}, \{T_{i,s,out}\}_{i=1}^N, T_{sep,out}, T_{c,out}$	$\{n_i^{H_2,an}\}_{i=1}^N, n_{liq}^{H_2,sep}, n_{gas}^{H_2,sep}$
Order of model	0	0	$N + 2$	$N + 3$
Formulation	(1)–(5)	(6)–(11)	(12)–(20)	(21)–(26)
Control variables	Electrolytic currents $\{I_i\}_{i=1}^N$, lye flow rates $\{v_{i,lye}\}_{i=1}^N$, and cooling water flow rates v_c			

system, the N -in-1 system features greater control freedom, as the current and lye flow distribution among the stacks can be adjusted. This increases the dimensionality of the control action space, making it more challenging to find the optimal control.

For the convenience, we summarize the state and control variables in vector forms:

$$\mathbf{x} \triangleq [T_{s,in}, T_{1,s,out}, \dots, T_{N,s,out}, T_{sep,out}, T_{c,out}, n_1^{H_2,an}, \dots, n_N^{H_2,an}, n_{liq}^{H_2,sep}, n_{gas}^{H_2,sep}]^T, \quad (27)$$

$$\mathbf{u} \triangleq [I_1, \dots, I_N, v_{1,lye}, \dots, v_{N,lye}, v_c]^T, \quad (28)$$

and compactly express the state equations as:

$$d\mathbf{x}/dt = \mathbf{h}(\mathbf{x}, \mathbf{u}). \quad (29)$$

4. Controller Design

4.1. Overview of Control

Section 3.3 shows that the N -in-1 AWE system is a complex multi-input multi-output (MIMO) system, making it challenging to ensure both safety and efficiency under fluctuating power inputs. Due to the MIMO characteristics and strong nonlinearity, PID [35, 36] or model predictive control (MPC) based on linearization are not suitable [60]. To address these challenges with full consideration of the nonlinear MIMO characteristics, this paper developed a nonlinear model predictive controller (NMPC) for the N -in-1 AWE system.

As in the classical MPC, we consider a control horizon N^h and a step length Δt for time-domain discretization. Given the large time constants of the temperature and HTO accumulation processes, typically on the order of tens of minutes, a longer horizon is required, and a large step length is desired to reduce the size of the optimization problem. Therefore, we use the trapezoidal format to discretize (29) in the time domain to ensure accuracy and numerical stability:

$$\frac{\mathbf{x}(k+1) - \mathbf{x}(k)}{\Delta t} = \frac{\mathbf{h}(\mathbf{x}(k+1), \mathbf{u}(k+1)) + \mathbf{h}(\mathbf{x}(k), \mathbf{u}(k))}{2}, \quad k = 0, \dots, N^h - 1, \quad (30)$$

Additionally, the control objectives and constraints are established as follows.

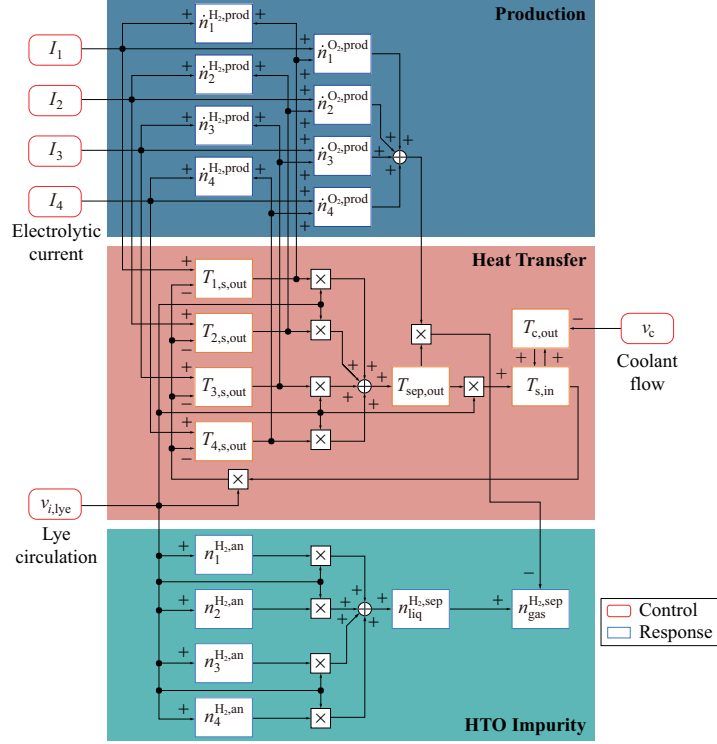


Figure 3: Interrelationships between state variables, control, and responses in the N -in-1 AWE system with the 1-pump topology in Fig. 2(c).

4.2. Control Objective

The primary control objective is to maximize hydrogen production while tracking the fluctuating energy input. Meanwhile, stack temperature should be stabilized to reduce thermal stress, and repeated adjustments of lye/cooling water flow should be minimized to alleviate fatigue. To achieve these goals, the overall objective function of the controller is set as:

$$\begin{aligned}
f(\mathbf{x}(1), \dots, \mathbf{x}(N^h), \mathbf{u}(0), \mathbf{u}(1), \dots, \mathbf{u}(N^h)) = & -\lambda^{\text{prod}} \Delta t \sum_{k=0}^{N^h} \sum_{i=1}^N \dot{n}_i^{\text{H}_2, \text{prod}} \\
& + \lambda^{\text{track}} \sum_{k=0}^{N^h} \left(P_{\text{tot}}^{\text{ref}}(k) - \sum_{i=1}^N P_i^{\text{ele}}(k) \right)^2 \\
& + \lambda^{\text{temp}} \sum_{k=0}^{N^h} \sum_{i=1}^N \left(T_{i, \text{s}, \text{out}}(k) - T_{\text{s}, \text{out}}^{\text{ref}} \right)^2 \\
& + \lambda^{\text{I}} \sum_{k=0}^{N^h-1} \sum_{i=1}^N \left(I_i(k+1) - I_i(k) \right)^2 \\
& + \lambda^{\text{lye}} \sum_{k=0}^{N^h} \sum_{i=1}^N \left(v_{i, \text{lye}}(k) - v_{i, \text{lye}}^0 \right)^2 \\
& + \lambda^{\text{c}} \sum_{k=0}^{N^h} \left(v_{\text{c}}(k) - v_{\text{c}}^0 \right)^2, \tag{31}
\end{aligned}$$

where $P_{\text{tot}}^{\text{ref}}$ is the reference for total power consumption; $T_{\text{s}, \text{out}}^{\text{ref}}$ is the temperature reference for the i th stack; λ^{prod} , λ^{track} , λ^{temp} , λ^{I} , λ^{lye} , and λ^{c} are weights for hydrogen production, load tracking, temperature

stabilization, and electrolytic current, lye circulation and cooling water flow adjustments.

For power tracking, i.e., the second row in (31), three application scenarios are considered:

1. Tracking renewable energy. Forecasts of wind and solar power are used as the power reference $P_{\text{tot}}^{\text{ref}}(k)$, and the forecast error is alleviated through the rolling implementation of NMPC. Techniques such as robust control [53] can be used to improve performance under uncertainty.
2. Participating in peak-shaving for the power grid: Power references are issued by grid operators in advance, which is a deterministic time series.
3. Tracking automatic generation control (AGC) signals: Given the high uncertainty, non-Gaussian characteristics, and temporal correlations of AGC signals, the dynamic response of the AWE system should be treated as a stochastic process and addressed with stochastic MPC (SMPC), as demonstrated in prior studies [61, 62]. Since this paper focuses on the AWE system, deterministic power references are considered, leaving SMPC for future research.

4.3. Constraints

At each time step ($k = 1, \dots, N^{\text{h}}$) and for each stack ($i = 1, \dots, N$), the following constraints must be satisfied to ensure operational feasibility and safety.

4.3.1. DC Power and Cell Voltage Constraints

The rectifier that provides DC power has current and power limits, expressed as:

$$0 \leq I_i^{\text{cell}}(k) \leq \bar{I}, \text{ and } 0 \leq P_i^{\text{ele}}(k) \leq \bar{P}^{\text{ele}}, \quad (32)$$

where \bar{I} and \bar{P}_i^{ele} are the current and power limits that the rectifier can provide, which is usually 1.2 to 1.4 times the rated power of the stack.

Moreover, to avoid excessive stress on electrodes and catalysts, the cell voltage is limited:

$$U_i^{\text{cell}}(k) \leq \bar{U}^{\text{cell}}, \quad (33)$$

where \bar{U}^{cell} is typically set at 2.1 to 2.3 V.

Note that some studies [9–13] and [48] set a non-zero lower power limit to avoid HTO over-limit under low loads. However, HTO accumulation is a dynamic process. Setting non-zero lower current or power limits independently is prone to being conservative by excluding short-term low-load operations [52]. This work integrates HTO dynamics into the controller to exploit flexibility, eliminating the need for non-zero lower power limits.

4.3.2. Hydrogen Production and Ramp Constraints

In order to avoid sudden changes in pressure, the gas-liquid ratio in the stacks, the liquid levels in separators, etc., which could induce structural stress, the hydrogen production rate is subject to ramp constraints:

$$r^{\text{H}_2, \text{prod}, \text{down}} \leq \frac{\dot{n}_i^{\text{H}_2, \text{prod}}(k) - \dot{n}_i^{\text{H}_2, \text{prod}}(k-1)}{\Delta t} \leq r^{\text{H}_2, \text{prod}, \text{up}}, \quad (34)$$

where $r^{\text{H}_2, \text{prod}, \text{up}}$ and $r^{\text{H}_2, \text{prod}, \text{down}}$ are the upward and downward ramp limits, respectively.

4.3.3. Temperature and HTO Constraints

Based on the dynamic model presented in Sections 3.2.2 and 3.2.3 and the following constraints, we can ensure that the temperature and HTO impurity concentration stay within safe levels:

$$T_{i, \text{s}, \text{out}}(k) \leq \bar{T}, \text{ and } \text{HTO}(k) \leq 2\%. \quad (35)$$

4.3.4. Lye and Coolant Flow Constraints

Due to the limitations of pump load, valve opening range, cold water inlet pressure, etc., the lye flow and cooling water flow must also be controlled within the feasible range, as:

$$\underline{v}_{\text{lye}} \leq v_{i, \text{lye}}(k) \leq \bar{v}_{\text{lye}}, \text{ and } \underline{v}_c \leq v_{i, c}(k) \leq \bar{v}_c, \quad (36)$$

where $\underline{v}_{\text{lye}}$, \bar{v}_{lye} and \underline{v}_c , \bar{v}_c denote the respective lower and upper limits of lye and coolant flow rates.

4.4. Simplification of Nonlinear Components

The complete state-space model developed in Section 3 is highly nonlinear and non-convex, making direct integration into NMPC computationally infeasible. To address this, the following simplifications are made.

4.4.1. Polyhedral Approximation of Production Function and Electrolytic Heat

From the models (1)–(5) in Section 3.1, it can be seen that the current, temperature, electrical power, and hydrogen flow show strong nonlinearity. Fortunately, if the relationship between power and gas production is relaxed into the form of inequality constraints:

$$\dot{n}_i^{\text{H}_2, \text{prod}}(I_i, T_{i, \text{s}}) \leq \frac{\eta_i^{\text{cell}}(I_i, T_{i, \text{s}}) P_i^{\text{ele}}(I_i, T_{i, \text{s}})}{2F N^{\text{cell}} U_i^{\text{cell}}(I_i, T_{i, \text{s}})}, \quad (37)$$

$$\dot{n}_i^{\text{O}_2, \text{prod}}(I_i, T_{i, \text{s}}) \leq \frac{\eta_i^{\text{cell}}(I_i, T_{i, \text{s}}) P_i^{\text{ele}}(I_i, T_{i, \text{s}})}{4F N^{\text{cell}} U_i^{\text{cell}}(I_i, T_{i, \text{s}})}, \quad (38)$$

then it is easy to find that the feasible space defined by (37)–(38) are convex. Further considering the control objective (31), that is, to maximize $\dot{n}_i^{\text{H}_2, \text{prod}}$, and $\dot{n}_i^{\text{O}_2, \text{prod}}$, when the NMPC obtains the optimal solution, (37)–(38) all take the equality, that is, the above relaxation is exact.

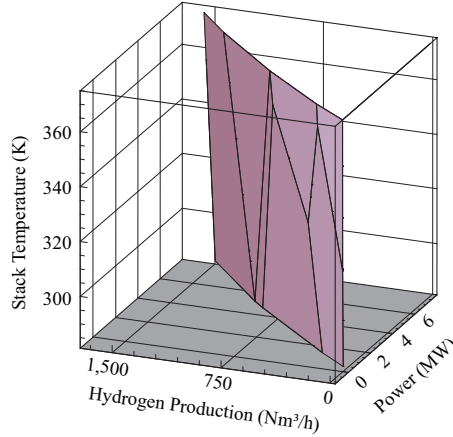


Figure 4: Polyhedral approximation of the production function of a 1,000 Nm³/h-rated stack.

Then, we use the double description (DD) algorithm [63] to find the optimal polyhedral approximation of the feasible space defined by (37)–(38), formulated as a linear inequality:

$$\left[\dot{n}_i^{\text{H}_2, \text{prod}}, \dot{n}_i^{\text{O}_2, \text{prod}} \right]^T \leq \mathbf{A} \left[P_i^{\text{ele}}, T_{i, \text{s}} \right]^T + \mathbf{b}, \quad (39)$$

where \mathbf{A} and \mathbf{b} are constant matrix and vector. Use a 1,000 Nm³/h-rated stack studied in Section 5 as an example, with an error tolerance taken as 0.1%, Fig. 4 shows the polyhedral approximation. We use (39) to replace the original model (1)–(5) in the controller, thereby eliminating non-convexity.

4.4.2. Reduced-Order Approximation of the HTO Accumulation Process

As discussed in Section 3.2.3, the process of HTO accumulation takes three stages. The time constants for the anode half-cell and liquid phase of the separator are on the orders of seconds and minutes, while the gas-phase time constant ranges to tens of minutes. Thus, we can focus solely on the gas phase and adopt a first-order model to approximate the entire process:

$$\frac{dn_{\text{gas}}^{\text{H}_2, \text{sep}}}{dt} = \sum_{i=1}^N \dot{n}_i^{\text{H}_2, \text{im}} - \dot{n}_{\text{out}}^{\text{H}_2}. \quad (40)$$

Replacing (24) with (40), the order of the model is reduced from $N+2$ to 1, improving both computational efficiency and numerical stability. Additionally, the molar quantity of HTO impurities in the half-cells and liquid phase, $n_i^{\text{H}_2, \text{an}}$ and $n_{\text{liq}}^{\text{H}_2, \text{sep}}$, cannot be measured. After simplification, these variables are omitted, with the remaining $n_{\text{gas}}^{\text{H}_2, \text{sep}}$ easily measurable, thereby eliminating the need for a state estimator.

Remark 2. *The time constants of the heat transfer processes among stacks, separators, and the heat exchanger do not differ by order of magnitude. Therefore, unlike the HTO process, reducing the order of the temperature dynamic model would introduce noticeable errors. This has been discussed in studies on 1-in-1 systems [34], and the same applies to N-in-1 systems.*

4.4.3. Bilinear Terms in Temperature and Mass Transfer Dynamics

The state-space model presented in Section 3 has bilinear terms, which cannot be relaxed as convex as in Section 4.4.1. To address these terms, we employ a discretization-based big-M method [64].

The bilinear terms requiring reformulation include $I_i T_{i,s}$, I_i^2 , $I_i n_{\text{gas}}^{\text{H}_2, \text{sep}}$, $v_{i, \text{lye}} T_{i,s}$, $v_{i, \text{lye}} T_{\text{sep}, \text{out}}$, and $v_c T_{c, \text{out}}$. Taking $I_i T_{i,s}$ as an example, the following steps are applied. First, discretize I_i as

$$I_i = \sum_{k=1}^{N^d} 2^{k-1} \beta_{i,k}^I \Delta I, \quad (41)$$

where N^d is the number of binary bits; $\Delta I = \bar{I}/2^k$ is the step size; and $\beta_{i,k}^I$ represents the k th binary variable. Then, $I_i T_{i,s}$ can then be replaced with:

$$I_i T_{i,s} = \sum_{k=1}^{N^d} 2^{k-1} \delta_{i,k}^{I,T} \Delta I, \quad (42)$$

$$T_{i,s} - M(1 - \beta_{i,k}^I) \leq \delta_{i,k}^{I,T} \leq T_{i,s} + M(1 - \beta_{i,k}^I), \quad (43)$$

$$-M\beta_{i,k}^I \leq \delta_{i,k}^{I,T} \leq M\beta_{i,k}^I, \quad (44)$$

where $\delta_{i,k}^{I,T}$ is an intermediate variable; M is a sufficiently large constant. This reformulation converts bilinear terms into mixed-integer linear constraints, which can be efficiently solved using commercial solvers.

4.4.4. Controller Summary

After the aforementioned simplification, the optimization model in the NMPC is transformed as a mixed-integer quadratic programming (MIQP) problem, expressed compactly as:

$$\max (31), \text{ s.t. } (30), (39), (33)\text{--}(36), (41)\text{--}(44). \quad (45)$$

With the simplified model, we can set a control horizon ranging from a few minutes to an hour, and the step length to several minutes. Under these conditions, solving the NMPC takes only a few seconds, meeting real-time operation requirements.

During implementation, as in standard MPC procedures, (45) is solved every few seconds based on the power reference and measurements of temperature and HTO impurity concentration. The first step of the obtained control series is applied. By repeating this process, the N -in-1 system dynamically allocates power among the N stacks, and adjusts lye circulation and cooling water flow rates, achieving load tracking, temperature stabilization, and suppression of HTO accumulation under dynamic power input. During this process, the pressure and liquid levels are regulated by a separated controller, which is not covered in this work, as noted by Assumption A in Section 2.2.

Remark 3. *The NMPC proposed here not only targets the optimal control of N -in-1 systems but also aims to provide a fair ground for the performance comparison among N -in-1 systems with different lye distribution topologies and the 1-in-1 system, as the controller can easily adapt to different configurations by slightly modifying the integrated state-space model while preserving optimality. Leveraging it, we can answer the Question 1 raised in the Introduction; see Sections 5.4–5.6.*

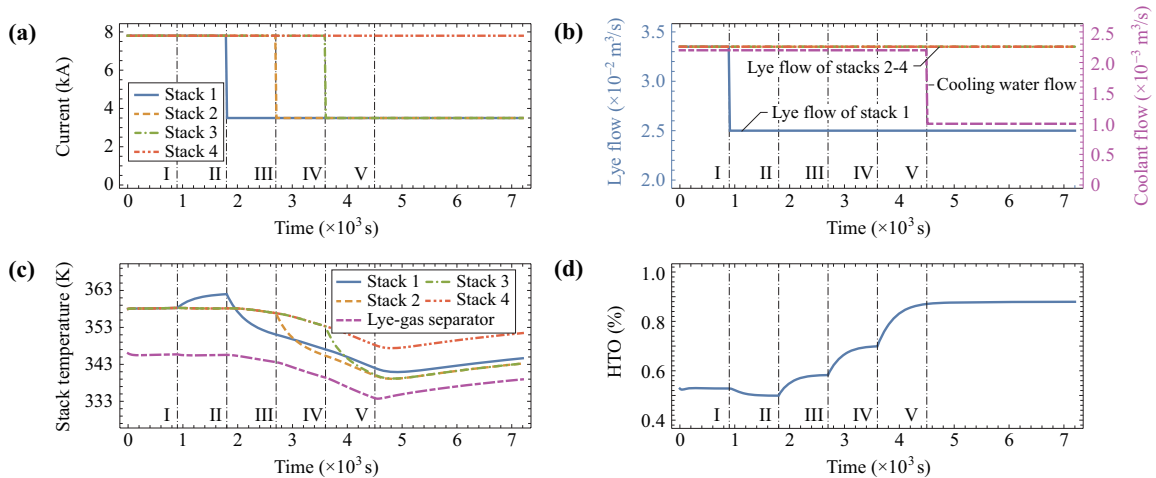


Figure 5: Open-loop responses of the 4-in-1 AWE system. (a) Electrolytic currents of the stacks. (c) Lye flow rates of the stacks and Cooling water flow rate. (c) Temperature of the stacks and separator; (d) HTO impurity at the gas phase of the separator.

5. Simulation Studies

5.1. Simulation System Setup

A 4-in-1 configuration, commonly used in real-world projects [15, 16], is selected for analysis. The nominal production rate of the system is set to 4,000 Nm³/h, with each stack to be 1,000 Nm³/h. The stack parameters are based on a test platform with a 1-in-1 configuration in *Beijing Power Equipment Group in China* [47], while the parameters of the BoP are scaled proportionally. The parameters used in the simulation are detailed in Table A1 in Appendix A.

For the controller setup, the horizon and step length are set as $N^h = 1,800$ s and $\Delta t = 450$ s. The weight coefficients in the objective function (31) are set as $\lambda^{\text{prod}} = 1$, $\lambda^{\text{track}} = 1.2$, $\lambda^{\text{temp}} = 0.15$, $\lambda^I = 0.0002$, $\lambda^{\text{lye}} = 25,000$, and $\lambda^c = 0.5$. The complete model presented in Section 3 and Table 2 is used for time-domain simulation, preserving all nonlinear dynamic processes. The NMPC updates the control commands every 10 seconds based on the optimization model summarized in Section 4.4.4. Simulations are performed on *Wolfram Mathematica 13.0*, and the optimization problem in the controller is solved via *Gurobi 11.0.3*.

5.2. Open-Loop Simulation

An open-loop simulation is conducted without the feedback controller to demonstrate the cross-coupling relationships between control (i.e., current, lye flow rate, and cooling water flow rate) and responses (such as temperature and HTO impurity concentration), as shown in Fig. 3. The system employs the 4-pump configuration shown in Fig. 2(a), allowing independent adjustment of the lye flow rate for each stack. The initial conditions are set as follows: stack temperature at 85 °C (358 K), separator temperature at 73 °C

(345 K), and HTO concentration at 0.52%. The control actions for current, lye flow, and cooling water flow are plotted in Fig. 5(a) and 5(b).

We can observe that, at 900 s, when the lye flow rate of stack 1 steps down from $3.35 \times 10^{-2} \text{ m}^3/\text{s}$ to $2.5 \times 10^{-2} \text{ m}^3/\text{s}$ (Action I), the temperature of stack 1 rises while the HTO concentration decreases slightly by 0.5 K. At 1,800 s, 2,700 s, and 3,600 s, the electrolytic currents of stacks 1–3 successively step down from 7,800 A to 3,500 A (Actions II, III, and IV), which leads to temperature drops in these stacks and a gradual decline in separator temperature to 333.4 K (60.4 °C.) while the HTO concentration increases from 0.50% to 0.84%. Finally, at 4,500 s, the cooling water flow rate is reduced from $2.2 \times 10^{-3} \text{ m}^3/\text{s}$ to $1.0 \times 10^{-3} \text{ m}^3/\text{s}$ (Action V), leading to a simultaneous temperature increase across all components, with a magnitude of 5.5 K in 2,500 s. Temperature variations directly affect cell voltages, electrolytic heat, and other states. The results highlight complex inter-couplings within the N -in-1 AWE system shown in Fig. 3, emphasizing the necessity of considering MIMO characteristics in the controller design.

5.3. Overall Performance under Dynamic Operation

The performance of the 4-in-1 system under the proposed NMPC is analyzed. The simulation adopts the 4-pump configuration shown in Fig. 2(a). The load reference $P_{\text{tot}}^{\text{ref}}(t)$ emulates the fluctuations of renewable energy ranging from 6 MW to 38 MW, shown in Fig. 6(a), and the simulation lasts for 8 hours. During the first 5 hours, the load reference fluctuates at a lower level, followed by 3 hours of high power supply, allowing a comprehensive evaluation of the dynamic operation of the AWE system.

The initial temperatures of stacks are set to 85 °C, 70 °C, 55 °C, and 40 °C (358 K, 343 K, 328 K, and 313 K), respectively. The separator temperature is set to 65 °C (338 K), with an initial HTO concentration at 1.2%. Throughout the simulation, the controller continuously adjusts the current, lye flow, and cooling water flow for each stack, as shown in Fig. 6(b)–(d), and the behaviors of the 4-in-1 system are discussed.

a) Inter-stack Load Allocation: The load is evenly shared among the 4 stacks throughout the process. This is driven by the objective function (31), which maximizes hydrogen yield. As shown in Fig. 4, the relation between hydrogen yield, electrolytic power, and temperature is concave. At the point of maximum hydrogen yield, the partial derivatives of the production rate with respect to power consumption across all stacks are equal, i.e., $\partial \dot{n}_i^{\text{H}_2, \text{prod}} / \partial P_i^{\text{ele}} = \partial \dot{n}_j^{\text{H}_2, \text{prod}} / \partial P_j^{\text{ele}}, \forall i, j \leq N$. With the stacks to be identical, this leads to an even power distribution, a phenomenon known as the *equimarginal principle*, discussed in our previous work for scheduling multiple electrolyzers [53, 57]. After 20,000 s, when the power supply exceeds the rectifiers' total power limit, i.e., 24 MW, all stacks operate at full load, saturating hydrogen production rates.

b) Temperature Dynamics: Due to interconnection via the BoP, heat exchange occurs between the stacks, stack temperatures quickly reach uniformity at the setpoint, 85 °C. As shown in Figs. 6(c) and 6(e), stacks 4 and 3, initially cooler than the separator, increase their lye flow rates to accelerate heating, while stacks 1

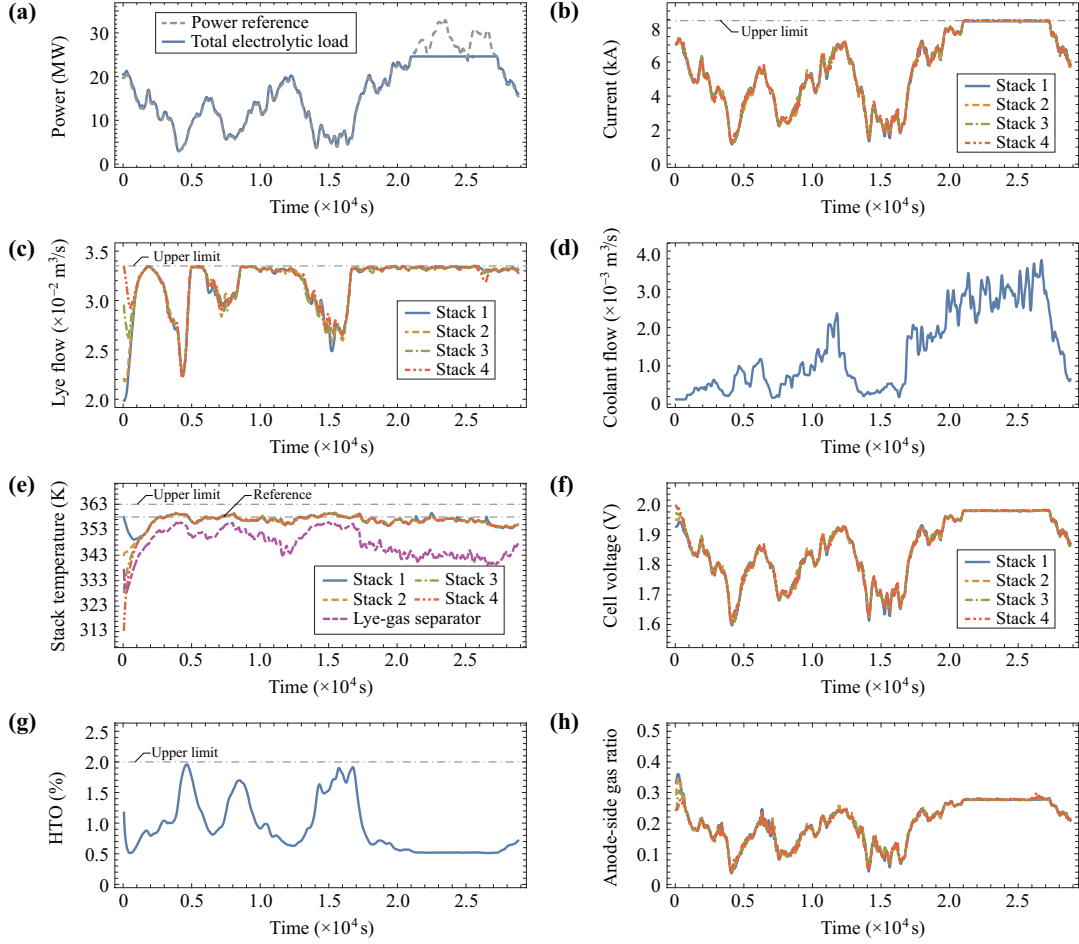


Figure 6: Control and responses of the 4-in-1 AWE system with a 4-pump configuration. (a) Load power reference and overall power consumption. (b) Electrolytic currents of the stacks. (c) Lye flow rates of the stacks. (d) Cooling water flow rate. (e) Temperature of the stacks and separator. (f) Cell voltage of the stacks. (g) HTO impurity at the gas phase of the separator. (h) Gas ratio in the anode half-cells.

and 2 reduce lye flow rates to minimize heat loss. The lowest flow rates for stacks 1 and 2 reach $0.0195 \text{ m}^3/\text{s}$ and $0.0218 \text{ m}^3/\text{s}$ compared to the rated value of $0.0345 \text{ m}^3/\text{h}$. Heat exchange rapidly makes stack temperatures reach unison during startup. For the rest of the time, lye flow adjustments are minimized to avoid excessive fluctuations that could affect the gas-liquid ratio, and temperature control mainly relies on cooling water adjustments, making the stack temperature stay within a range of $[81, 86] \text{ C}^\circ$.

c) HTO Accumulation Dynamics: Since HTO impurity concentration is not included in the objective (31) but in the inequality constraints, the fluctuations in HTO impurity do not affect the control actions in most cases. However, during significant load drops (e.g., at 4,000 s, 8,000 s, and 15,000 s), the HTO concentration rises rapidly, which is similar to 1-in-1 systems. To prevent exceeding the safety limit 2%, the controller reduces lye flow rates to $0.0225 \text{ m}^3/\text{s}$, $0.0285 \text{ m}^3/\text{s}$, and $0.0250 \text{ m}^3/\text{s}$ (67%, 85%, and 75% of the

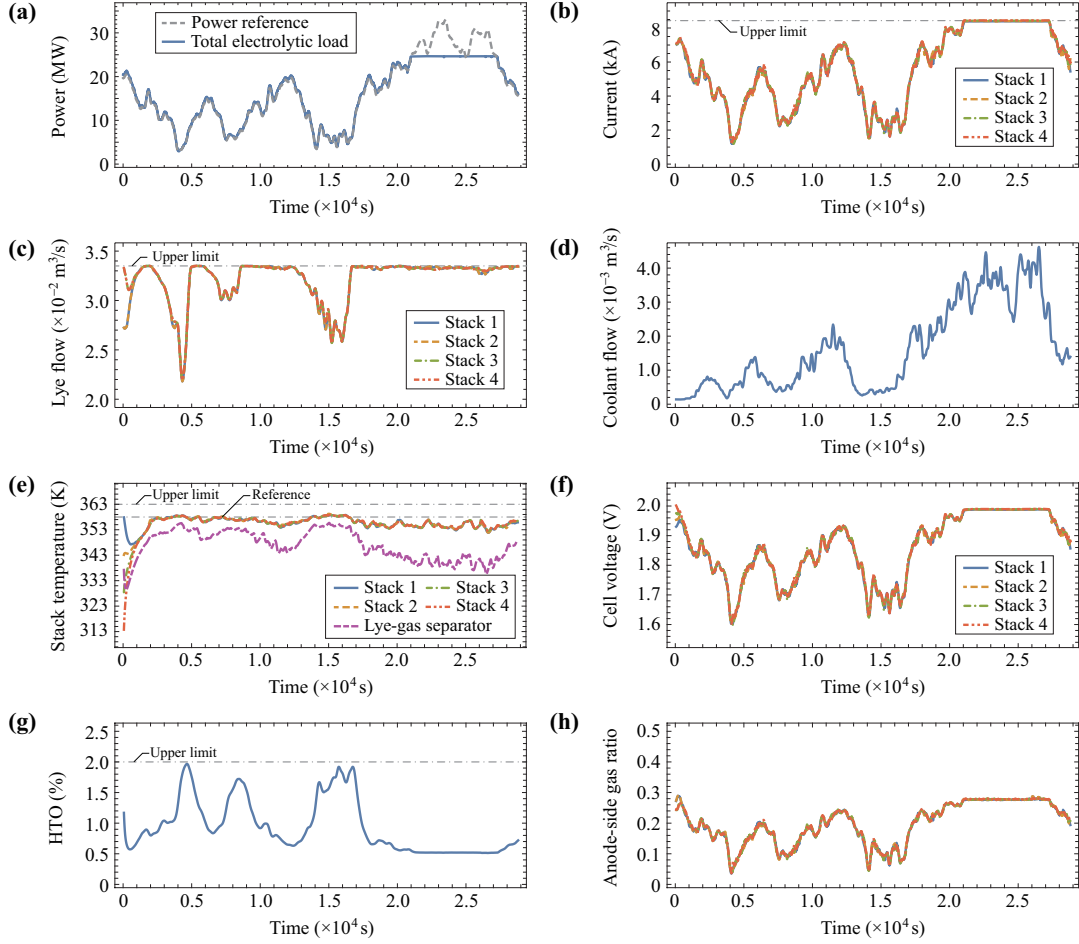


Figure 7: Control and responses of the 4-in-1 AWE system with a 2-pump configuration shown in Fig. 2(b). (a) Load power reference and overall power consumption. (b) Electrolytic currents of the stacks. (c) Lye flow rates of the stacks. (d) Cooling water flow rate. (e) Temperature of the stacks and separator; (f) Cell voltage of the stacks. (g) HTO impurity at the gas phase of the separator. (h) Gas ratio in the anode half-cells.

rated value) respectively, mitigating lye circulation-induced HTO cross-mixing, which is modeled by (22). Elsewhere, to stabilize the gas-liquid ratio, the lye flow is kept near its rated value, as shown in Fig. 6(f).

These results demonstrate that despite that the hydrogen yield, temperature, and HTO concentration are tightly coupled in the N -in-1 system, as shown in Fig. 3 and exemplified in Section 5.2, the proposed controller can manage these complexities effectively, thereby answering Question 2 posed in Section 1.1.

5.4. Comparisons Between Different Lye Circulation Topologies

As discussed in Section 3.2.1, the degree of freedom in controlling lye flow distribution varies across different topologies. To evaluate their impact on the performance of the AWE system under varying loads, this section performs simulations with the three topologies in Fig. 2, using the load power reference shown in Fig. 6(a). All other parameters of the AWE system and controller remain constant.

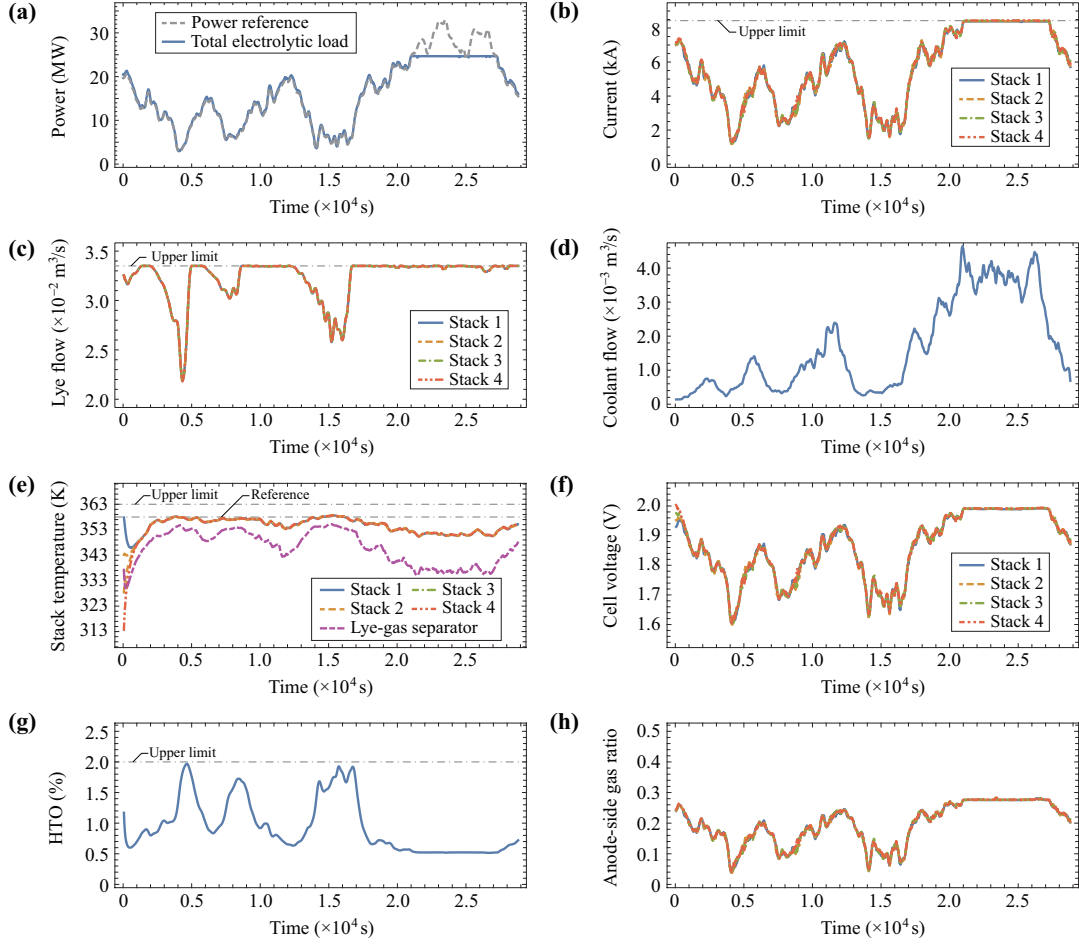


Figure 8: Control and responses of the 4-in-1 AWE system with a 1-pump configuration shown in Fig. 2(c). (a) Load power reference and overall power consumption. (b) Electrolytic currents of the stacks. (c) Lye flow rates of the stacks. (d) Cooling water flow rate. (e) Temperature of the stacks and separator; (f) Cell voltage of the stacks. (g) HTO impurity at the gas phase of the separator. (h) Gas ratio in the anode half-cells.

Figs. 7 and 8 present the 8-hour simulation results for the 2-pump and 1-pump configurations, respectively. Apart from the differences in inter-stack lye flow distribution during the startup phase, the control commands for electrolytic current, cooling water flow, and performance metrics (including load tracking, temperature stabilization, and suppression of HTO concentration) are nearly identical across all configurations, with no significant differences observed.

To further analyze the transient behavior of AWE systems with different topologies, the control of lye flow and the temperature responses during the first 30 minutes are shown in Fig. 9. In the 4-pump topology, lye flow rates in the stacks decrease by large and differing levels first and rise afterward, as analyzed in Section 5.3. In contrast, in the 2-pump and 1-pump configurations, stacks sharing a common circulation pump exhibit nearly identical lye flow rates, which cannot be independently adjusted, as noted in Section

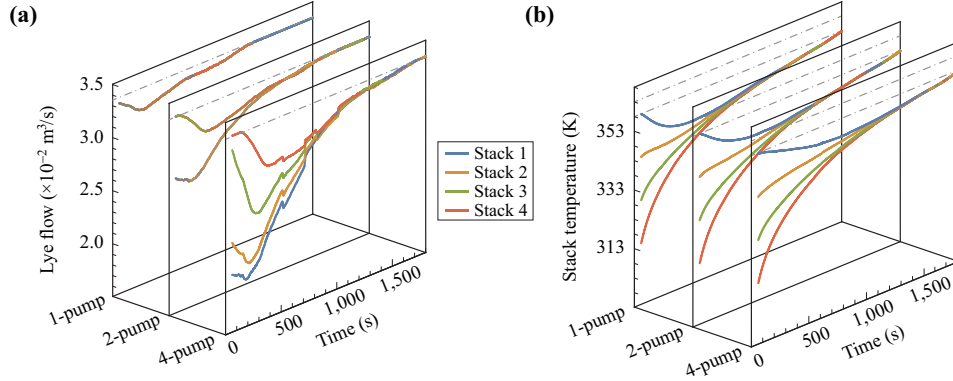


Figure 9: Comparison on control and responses of the 4-in-1 AWE system with 1-pump, 2-pump, and 4-pump configurations. (a) Lye flow rates of the stacks. (b) Temperature of the stacks.

Table 3: Performance comparison between 4-in-1 AWE systems with different lye circulation topologies and four 1-in-1 systems operating in parallel

Configuration	Energy use (MWh)	Load-tracking RMSE (MW)	Load-tracking RMSE for first 5 hours (MW)	RMSE for stack temperature control (K)	Total hydrogen yield (Nm^3)	Specific energy consumption (kWh/Nm^3)
4-in-1 (4-pump)	124.495	2.151	0.379	3.599	24,007.2	5.186
4-in-1 (2-pump)	124.521	2.148	0.379	4.055	23,997.9	5.189
4-in-1 (1-pump)	124.528	2.149	0.381	5.502	23,977.4	5.193
Four 1-in-1 systems	124.482	2.159	0.376	2.237	24,000.4	5.186

3.2.1 and Remark 1. Therefore, these systems cannot actively regulate inter-stack heat exchange through differential lye flow, and the controller instead maintains higher lye flow rates (higher than $0.0272 \text{ m}^3/\text{s}$ and $0.0318 \text{ m}^3/\text{s}$ for the 2-pump and 1-pump configurations, respectively) across all stacks to accelerate the process of reaching temperature unison.

As a result, the temperatures of stacks 1 and 2 in the 2-pump and 1-pump configurations drop significantly (10.5 K and 12 K for stack 1 in the 2-pump and 1-pump systems), reducing energy conversion efficiency. In the 4-pump configuration, however, the temperature drops for stacks 1 and 2 are mitigated (8.5 K for stack 1) due to independent lye flow control. After the startup phase, temperatures across all four stacks in all configurations converge at the setpoint 85 C° , and lye flow rates return to their rated values. From this point on, as shown in Figs. 6, 7, and 8, there are no significant differences.

These results highlight that differences in lye circulation topology can lead to notable variations in transient characteristics. Nevertheless, the proposed NMPC effectively accommodates these differing characteristics by optimizing multiple control actions from a global perspective, achieving similar performances.

Table 3 summarizes key performance metrics, including the electricity consumption, hydrogen yield, load tracking deviation, and energy consumption over the entire 8-hour simulation. Due to the reduced control

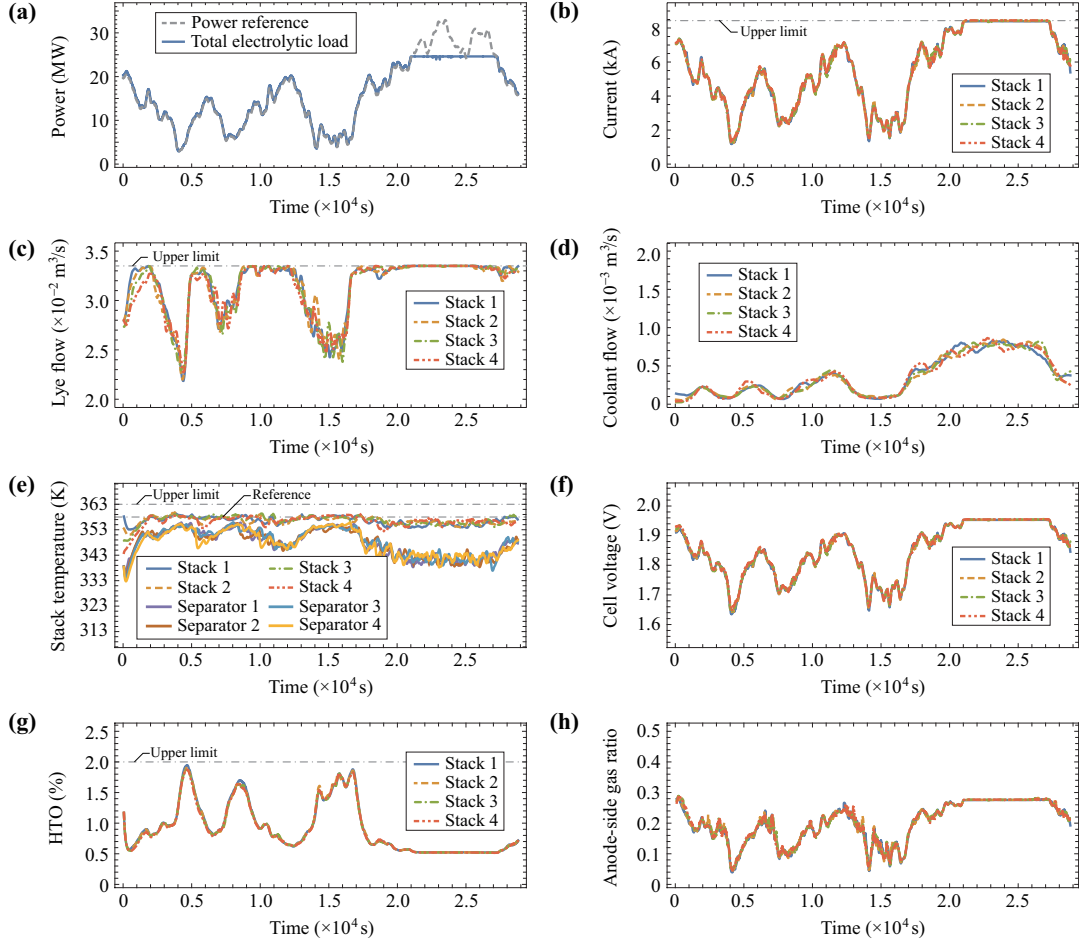


Figure 10: Control and responses of four traditional 1-in-1 AWE systems operating in parallel. (a) Load power reference and overall power consumption. (b) Electrolytic currents of the stacks. (c) Lye flow rates of the stacks. (d) Cooling waters flow rate. (e) Temperature of the stacks and separators; (f) Cell voltage of the stacks. (g) HTO impurity at gas phase of the separator. (h) Gas ratio in the anode half-cells.

flexibility in the 2-pump and 1-pump configurations, we can observe slight increases in the temperature control RMSE by 0.456 and 1.903 K and marginal increases in specific energy consumption by 0.003 and 0.007 kWh/Nm³, respectively, compared to the 4-pump configuration. Nevertheless, as the proposed controller can adapt to varying conditions, the absolute differences in the metrics are minimal, and the relative differences are less than 0.13%, which may not be noticeable in the application. In conclusion, under reasonable control, the impact of lye circulation topology on overall performance is negligible.

5.5. Comparing the N -in-1 System with Multiple 1-in-1 AWE Systems

Considering the Question (a) posed Section 1.1, while many ReP2H projects have invested in N -in-1 AWE systems, academic research has predominantly focused on 1-in-1 systems. To fill this gap, it is essential

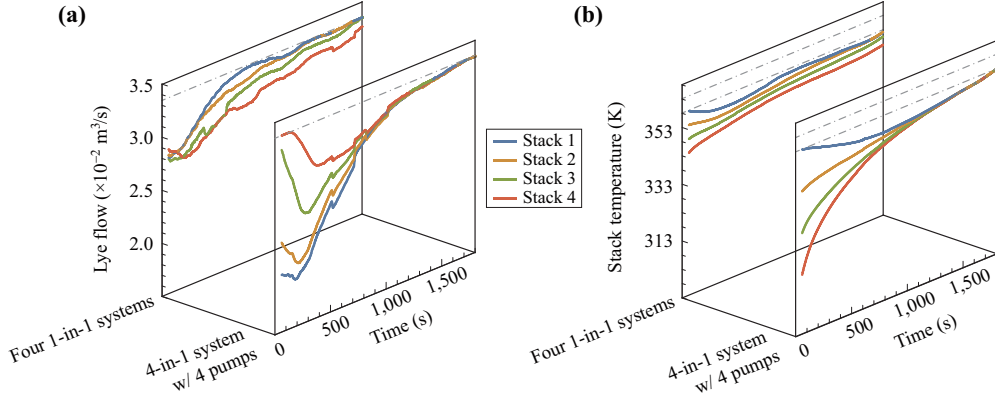


Figure 11: Comparison on control and responses between the 4-in-1 AWE system with a 4-pump configuration and four traditional 1-in-1 system in parallel. (a) Lye flow rates of the stacks. (b) Temperature of the stacks.

to analyze the differences between these two configurations in terms of flexibility, energy efficiency, and other aspects. This section conducts a comparative study to address these differences.

The 4-in-1 system with a $4,000 \text{ Nm}^3/\text{h}$ -rated capacity, as described in Section 5.1, is compared with four 1-in-1 systems operating in parallel, each with a $1,000 \text{ Nm}^3/\text{h}$ rated capacity, given the load reference signal shown in Fig. 6(a). Parameters for the 1-in-1 systems are also based on the test platform at *Beijing Power Equipment Group* [47]. The stack settings for the 1-in-1 systems are identical to those of the 4-in-1 system, with the parameters of BoP components scaled proportionally to $1/N$ of the 4-in-1 system. For a fair comparison, the 1-in-1 systems are also controlled using the proposed NMPC, with N set to 1 and other settings unchanged. Given that AWE systems require 40 minutes to 1 hour for a full cold startup, and the focus here is on the varying-load operation, we assume that all four 1-in-1 systems remain in operation. Startup and shutdown scheduling is excluded and left for future studies.

As in Section 5.3, the initial temperatures of the stacks in the 1-in-1 systems are set to $85 \text{ }^\circ\text{C}$, $70 \text{ }^\circ\text{C}$, $55 \text{ }^\circ\text{C}$, and $40 \text{ }^\circ\text{C}$, respectively, with the initial temperature of the separators to be $65 \text{ }^\circ\text{C}$, and the initial HTO concentration at 1.2%. Fig. 10 presents the simulation results for the four 1-in-1 systems, while Fig. 11 compares the lye flow control and temperature responses during the initial phase.

By comparing the results of the 4-in-1 system in Sections 5.3 and 5.4 with the 1-in-1 systems, we can find that the behaviors of the two configurations are largely similar. As discussed in Section 5.3, under the equimarginal principle, stacks evenly share power to maximize hydrogen production. In the 1-in-1 systems, the independence of temperature and lye flow control leads to nearly identical control actions under the same objectives.

A minor difference arises during the initial phase due to the absence of inter-stack heat exchange in the 1-in-1 systems. As shown in Fig. 11, the lack of differential lye flow control for temperature equalization results in gentler control actions for lye flow and temperature in the 1-in-1 systems. For the 4-in-1 system,

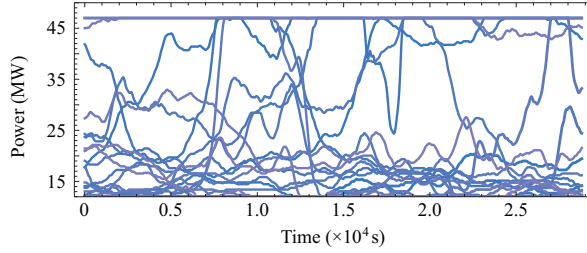


Figure 12: reference signals based on a wind farm by the Risø

the stack lye flow rates drop by 33% at most to $0.225 \text{ m}^3/\text{s}$, while for the 1-in-1 systems the maximal drop is by 18.5% to $0.273 \text{ m}^3/\text{s}$. However, as stack temperatures converge, these differences decay, though the stack temperatures in 1-in-1 system converge in a slower manner due to heat insulation among the stacks.

The performance metrics summarized in Table 3 also show that the efficiency, load-tracking performance, and other key indicators are nearly identical between the two configurations. The differences in load-tracking RMSE, stack temperature RMSE, and specific energy consumption are less than 0.010 MW, 3.265 K, and $0.007 \text{ kWh}/\text{Nm}^3$ even for the 1-pump configuration. This similarity suggests that the 4-in-1 system and 1-in-1 systems are interchangeable from a dynamic performance perspective. Therefore, as the answer to Question 1, employing the 4-in-1 system does not compromise flexibility or efficiency.

It is worth noting, however, that this study assumes all stacks in the N -in-1 system maintain an operational state. In practice, hydrogen plants with multiple 1-in-1 systems allow individual electrolyzers to start up and shut down independently, offering greater long-term flexibility [51–53]. For N -in-1 systems, constraints such as pressure and liquid level control may limit the operating range when not all the stacks are active. Additionally, the temperature or HTO impurity accumulation dynamics with partial stacks turned on may introduce new challenges. These issues warrant further investigation.

5.6. Comprehensive Comparisons under Various Scenarios

Finally, to comprehensively compare the N -in-1 and 1-in-1 configurations, simulations were conducted under 25 wind power supply scenarios. Each scenario, lasting 8 hours and shown in Fig. 12, is based on data from an offshore wind farm collected by Risø [49]. For each scenario, performance metrics, including total energy use, load-tracking RMSE, stack temperature control RMSE, total hydrogen yield, and specific energy consumption, are compared in Fig. 13. The average metrics are summarized in Table 4.

The results indicate that the performance of the 4-in-1 and 1-in-1 configurations under varying energy inputs is not significantly different, a conclusion consistent with the findings in Sections 5.4 and 5.5. We observe that, despite different power supply levels, the energy conversion efficiency remains nearly identical. Due to the constrained degree of freedom in lye flow control, the 4-in-1 systems with 2-pump and 1-pump configurations show a slightly higher RMSE in stack temperature stabilization, leading to a marginal

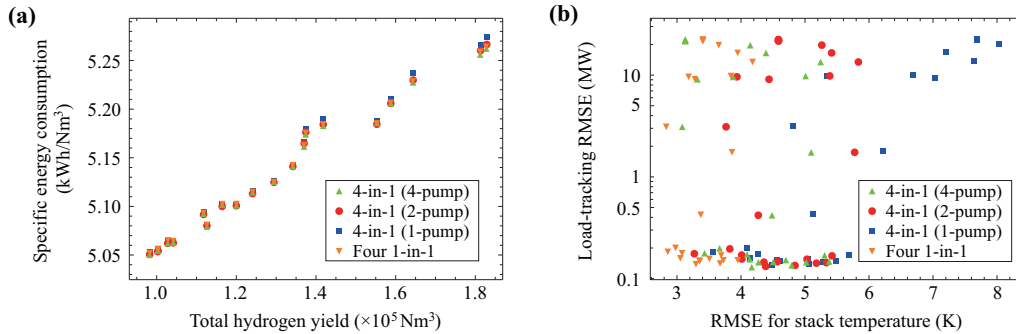


Figure 13: performance metrics of the 4-in-1 AWE systems with different lye circulation topologies and four 1-in-1 systems operating in parallel under 25 scenarios of wind power supply. (a) Total hydrogen yield and specific energy consumption. (b) RMSE for stack temperature and load-tracking RMSE.

Table 4: Average performance metrics of the 4-in-1 AWE systems with different lye circulation topologies and four 1-in-1 systems operating in parallel under 25 scenarios of wind power supply

Configuration	Energy use (MWh)	Load-tracking RMSE (MW)	RMSE for stack temperature control (K)	Total hydrogen yield (Nm^3)	Specific energy consumption (kWh/Nm^3)
4-in-1 (4-pump)	143.470	7.037	4.186	27,674.8	5.165
4-in-1 (2-pump)	143.495	7.030	4.667	27,670.0	5.167
4-in-1 (1-pump)	143.493	7.032	5.807	27,649.4	5.170
Four 1-in-1 systems	143.438	7.044	3.451	27,660.5	5.167

deterioration in energy conversion efficiency. The average differences in load-tracking RMSE, stack temperature RMSE, and specific energy consumption are below 0.014 MW, 2.356 K, and 0.003 kWh/Nm^3 . These increases can be negligible in practical applications.

In summary, we answer Question 1 by confirming that selecting the 4-in-1 system does not compromise flexibility or efficiency when compared to traditional 1-in-1 systems.

6. Conclusions

This paper proposes a state-space model for the N -in-1 AWE system, considering the dynamic behaviors of lye circulation, temperature, and HTO impurity accumulation. A controller based on NMPC is developed to coordinate inter-stack electrolytic current distribution, lye flow, and cooling, ensuring the N -in-1 system adapts to varying energy input.

Simulations across various scenarios with fluctuating wind energy input show that, despite the increased complexity and reduced control flexibility of the N -in-1 system, the proposed controller design allows the N -in-1 configuration with different lye circulation topologies to maintain similar energy conversion efficiency and flexibility compared to independent 1-in-1 systems.

Future research may address the following aspects. This study assumes continuous operation of the AWE system throughout the simulation period. For large hydrogen plants, the scheduling of electrolyzers, including on-standby-off state switching, should be further explored, along with a plant-wise performance comparison between the N -in-1 and 1-in-1 configurations. Additionally, the consideration of energy input uncertainty warrants further investigation.

Acknowledgement

The authors gratefully acknowledge the financial support from the National Key Research and Development Program of China (2021YFB4000503) and the National Natural Science Foundation of China (52377116 and 52307126).

Declaration of Interest

None.

Data Availability

The data related to this work are available upon request.

Appendix A: Parameters of the System Used in the Case Study

The parameters of the 4-in-1 AWE system used for simulations in Section 5 are presented in Table A1.

Table A1: Parameters of the 4-in-1 alkaline water electrolysis system used in the simulation

Parameter	Value
Number of stacks N	4
Rated hydrogen production	4,000 Nm ³ /h
Rated hydrogen production per stack	1,000 Nm ³ /h
Rated electrolytic current per stack I^{norm}	7,800 A
Maximal electrolytic current per stack \bar{I}	$1.2 \times I^{\text{norm}}$
Maximal stack power \bar{P}^{ele}	6 MW
Number of cells per stack N^{cell}	368
Cell area A_c	2 m ²
System pressure ρ	1.6 MPa
Differential pressure between half-cells $\Delta\rho$	0.1% ρ
Electrochemical parameters r_1, r_2, r_3, s	$3.202 \times 10^{-5} \Omega, 8.970 \times 10^{-8} \Omega/\text{K}, -4.193 \times 10^{-12} \Omega/\text{Pa}, 7.572 \times 10^{-2}$
Electrochemical parameters t_1, t_2, t_3	$-1.070 \times 10^{-1} \Omega, 14.43 \Omega \cdot \text{K}, 38.8 \Omega \cdot \text{K}^2$
Faraday efficiency parameters f_1, f_2	$50 + 2.5T_s \text{ (A}^2\text{)}, 0.92 - 6.25 \times 10^{-6}T_s$
Upper limit of cell voltage \bar{U}	2.1 V
Ramping limits $\bar{r}^{\text{H}_2, \text{prod}} / \bar{I}^{\text{H}_2, \text{prod}}$	$\pm 20 \text{ Nm}^3 / (\text{h} \cdot \text{s})$
Ambient temperature T_{am}	298 K (25 °C)
Coolant temperature $T_{c, \text{in}}$	288 K (15 °C)
Stack temperature reference $T_{s, \text{out}}^{\text{ref}}$	358 K (85 °C)
Stack temperature limit \bar{T}	363 K (90 °C)
Stack heat capacity $C_{i, s}$	$3.450 \times 10^7 \text{ J/K}$
Separator heat capacity C_{sep}	$5.193 \times 10^7 \text{ J/K}$
Heat capacity of heat exchanger C_{he}	$2.175 \times 10^7 \text{ J/K}$
Heat exchange area A_c	240 m ²
heat transfer coefficient k	980 W/K·m ²
Maximal cooling water flow rate \bar{v}_c	0.032 m ³ /s
Anode-side half-cell lye volume $V_{i, \text{lye}}^{\text{an}}$	2.5 m ³
Separator volume V_{sep}	10.288 m ³
Limits of lye flow rate per stack $\bar{v}_{\text{lye}}, \underline{v}_{\text{lye}}$	0.0335 m ³ /s, 0.0101 m ³ /s
Thickness of the diaphragm δ	$500 \times 10^{-6} \text{ m}$
Diffusion coefficient $D_{\text{eff}}^{\text{H}_2}$	$8.569 \times 10^{-10} \text{ m}^2/\text{s}$
Permeability coefficient $K_{\text{eff}}^{\text{H}_2}$	$2 \times 10^{-16} \text{ m}^2$
Separation time constant τ_{sep}	60 s

References

References

- [1] S. E. Hosseini, Hydrogen has found its way to become the fuel of the future, *Future Energy* 1 (3) (2022) 11–12.
- [2] International Energy Agency, *Global hydrogen review 2024* (Oct. 2024).
- [3] A. S. Emam, M. O. Hamdan, B. A. Abu-Nabah, E. Elnajjar, A review on recent trends, challenges, and innovations in alkaline water electrolysis, *Int. J. Hydrogen Energy* 64 (2024) 599–625.
- [4] H. Lange, A. Klose, L. Beisswenger, D. Erdmann, L. Urbas, Modularization approach for large-scale electrolysis systems: a review, *Sustainable Energy Fuels* (8) (2024) 1208–1224.
- [5] D. Niblett, M. Delpisheh, S. Ramakrishnan, M. Mamlouk, Review of next generation hydrogen production from offshore wind using water electrolysis, *J. Power Sources* 592 (2024) 233904.
- [6] Y. Chi, J. Lin, P. Li, Z. Yu, S. Mu, X. Li, Y. Song, Elevating the acceptable cost threshold for solid oxide cells: A case study on refinery decarbonization, *Appl. Energy* 373 (2024) 123829.
- [7] Q. Zhang, D. Xie, Y. Zeng, Y. Liu, H. Yu, S. Liu, Optimizing wind-solar hydrogen production through collaborative strategy with ALK/PEM multi-electrolyzer arrays, *Renew. Energy* 232 (2024) 121116.
- [8] C. Yang, J. Ma, G. Li, et al., Application and practice of many-to-one large-scale alkaline water electrolysis hydrogen production equipment, *Solar Energy* 5 (2022) 103–114, in Chinese.
- [9] M. Rizwan, V. Alstad, J. Jäschke, Design considerations for industrial water electrolyzer plants, *Int. J. Hydrogen Energy* 46 (75) (2021) 37120–37136.
- [10] M. Chen, J. Jia, B. Zhang, L. Han, M. Ji, Z. Yu, D. Li, W. Wang, H. Jia, H. Xu, Enhancing the efficiency of multi-electrolyzer clusters with lye mixer: Topology design and control strategy., *Energy Eng.* 121 (10).
- [11] Y. Shi, X. Hu, Z. Zhang, S. Lu, L. Xie, H. Su, Plant-wide modeling, design consideration, and practical hierarchical control strategy considering key variable integral characteristics for an industrial alkaline water electrolyzer plant, *Ind. Eng. Chem. Res.* 62 (36) (2023) 14441–14455.
- [12] T. Liang, M. Chen, J. Tan, Y. Jing, L. Lv, W. Yang, Large-scale off-grid wind power hydrogen production multi-tank combination operation law and scheduling strategy taking into account alkaline electrolyzer characteristics, *Renew. Energy* 232 (2024) 121122.
- [13] Y. Li, X. Deng, T. Zhang, S. Liu, L. Song, F. Yang, M. Ouyang, X. Shen, Exploration of the configuration and operation rule of the multi-electrolyzers hybrid system of large-scale alkaline water hydrogen production system, *Appl. Energy* 331 (2023) 120413.
- [14] X. Meng, A. Gu, J. Zeng, M. Chen, J. Zhou, B. Liu, Z. Mao, Advantages and challenges of China’s participation in international hydrogen trade, *Int. J. Hydrogen Energy* 52 (2024) 1356–1368.
- [15] A. Zhang, Y. Ma, R. Ding, L. Li, Alkaline water electrolysis at industrial scale, in: *Green Hydrogen Production by Water Electrolysis*, CRC Press, pp. 95–107.
- [16] Y. Zhai, Y. He, J. Shao, W. Zhang, X. Tong, Z. Wang, W. Weng, Review of hydrogen-driven power-to-x technology and application status in China, *Processes* 12 (7) (2024) 1518.
- [17] M. Sánchez, E. Amores, L. Rodríguez, C. Clemente-Jul, Semi-empirical model and experimental validation for the performance evaluation of a 15 kw alkaline water electrolyzer, *Int. J. Hydrogen Energy* 43 (45) (2018) 20332–20345.
- [18] D. Huang, B. Xiong, J. Fang, K. Hu, Z. Zhong, Y. Ying, X. Ai, Z. Chen, A multiphysics model of the compactly-assembled industrial alkaline water electrolysis cell, *Appl. Energy* 314 (2022) 118987.
- [19] N. Esfandiari, M. Aliofkhaezraei, A. N. Colli, F. C. Walsh, S. Cherevko, L. A. Kibler, M. M. Elnagar, P. D. Lund, D. Zhang, S. Omanovic, et al., Metal-based cathodes for hydrogen production by alkaline water electrolysis: Review of materials, degradation mechanism, and durability tests, *Progr. Mat. Sci.* (2024) 101254.

- [20] T. Wang, J. Wang, P. Wang, F. Wang, L. Liu, H. Guo, Non-uniform liquid flow distribution in an alkaline water electrolyzer with concave-convex bipolar plate (CCBP): A numerical study, *Int. J. Hydrogen Energy* 48 (33) (2023) 12200–12214.
- [21] M. Zhang, L. Gao, L. Yang, G. Shan, Y. Wang, X. Huo, W. Li, J. Zhang, Temperature distribution evolution in zero-gap alkaline water electrolyzer: Experimental and modeling, *Fuel* 367 (2024) 131418.
- [22] X. Cao, N. Zhao, S. Zhang, L. Zhou, Y. Hu, J. Yun, Investigation of the hydrogen bubble effect on the overpotential in an alkaline water electrolyzer, *Int. J. Hydrogen Energy* 49 (2024) 47–57.
- [23] R. Qi, M. Becker, J. Brauns, T. Turek, J. Lin, Y. Song, Channel design optimization of alkaline electrolysis stacks considering the trade-off between current efficiency and pressure drop, *J. Power Sources* 579 (2023) 233222.
- [24] G. Sakas, A. Ibáñez-Rioja, S. Pöyhönen, A. Kosonen, V. Ruuskanen, P. Kauranen, J. Ahola, Influence of shunt currents in industrial-scale alkaline water electrolyzer plants, *Renew. Energy* 225 (2024) 120266.
- [25] D. Dogan, B. Hecker, B. Schmid, H. Kungl, H. Tempel, R.-A. Eichel, Experimental determination of stray currents in parallel operated cells exemplified on alkaline water electrolysis, *Electrochimica Acta* 500 (2024) 144767.
- [26] J. Wang, Z. Ji, Z. Liu, Experimental and numerical investigation on the gas–liquid separation performance of a novel vane separator with grooves, *Chem. Eng. Res. Des.* 180 (2022) 306–317.
- [27] X. Zeng, G. Fan, J. Xu, A. Liu, Y. Xu, C. Yan, Experimental study on a new gas–liquid separator for a wide range of gas volume fraction, *Chem. Eng. Res. Des.* 160 (2020) 561–570.
- [28] Y. Hu, Z. Yin, C. Han, R. Tong, W. Li, H. Li, Study on gas-liquid separator for separation performance and structural optimization in AEL coupled with renewable energy sources, *Int. J. Hydrogen Energy* 88 (2024) 369–377.
- [29] S. Rashidi, N. Karimi, B. Sundén, K. C. Kim, A. G. Olabi, O. Mahian, Progress and challenges on the thermal management of electrochemical energy conversion and storage technologies: Fuel cells, electrolysers, and supercapacitors, *Prog. Energy Combust. Sci.* 88 (2022) 100966.
- [30] Y. Jiang, J. Wu, K. He, Y. Zhang, Q. Chen, M. Zhang, T. Zhao, Y. Liu, Performance analysis of alkaline water electrolysis system based on heat current modeling method, in: 2024 IEEE 2nd Int. Conf. Power Sci. Tech. (ICPST), IEEE, 2024, pp. 1785–1794.
- [31] L. Kang, X. Liang, Y. Liu, Optimal design of inter-plant hydrogen networks with intermediate headers of purity and pressure, *Int. J. Hydrogen Energy* 43 (34) (2018) 16638–16651.
- [32] Ø. Ulleberg, Modeling of advanced alkaline electrolyzers: a system simulation approach, *Int. J. Hydrogen Energy* 28 (1) (2003) 21–33.
- [33] M. David, H. Álvarez, C. Ocampo-Martínez, R. Sánchez-Peña, Dynamic modelling of alkaline self-pressurized electrolyzers: a phenomenological-based semiphysical approach, *Int. J. Hydrogen Energy* 45 (43) (2020) 22394–22407.
- [34] R. Qi, J. Li, J. Lin, Y. Song, J. Wang, Q. Cui, Y. Qiu, M. Tang, J. Wang, Thermal modeling and controller design of an alkaline electrolysis system under dynamic operating conditions, *Appl. Energy* 332 (2023) 120551.
- [35] R. Qi, J. Li, J. Lin, Y. Song, J. Wang, Q. Cui, Y. Qiu, M. Tang, J. Wang, Design of the pid temperature controller for an alkaline electrolysis system with time delays, *Int. J. Hydrogen Energy* 48 (50) (2023) 19008–19021.
- [36] R. Qi, X. Gao, J. Lin, Y. Song, J. Wang, Y. Qiu, M. Liu, Pressure control strategy to extend the loading range of an alkaline electrolysis system, *Int. J. Hydrogen Energy* 46 (73) (2021) 35997–36011.
- [37] H. Cheng, Y. Xia, W. Wei, Self-optimization control for alkaline water electrolyzers considering electrolyzer temperature variations, *IEEE Trans. Ind. Electronics*, Early Access.
- [38] Y. Li, T. Zhang, X. Deng, B. Liu, J. Ma, F. Yang, M. Ouyang, Active pressure and flow rate control of alkaline water electrolyzer based on wind power prediction and 100% energy utilization in off-grid wind-hydrogen coupling system, *Appl. Energy* 328 (2022) 120172.
- [39] Y. Li, T. Zhang, J. Ma, X. Deng, J. Gu, F. Yang, M. Ouyang, Study the effect of lye flow rate, temperature, system pressure and different current density on energy consumption in catalyst test and 500w commercial alkaline water electrolysis,

Materials Today Physics 22 (2022) 100606.

- [40] S. Ding, B. Guo, S. Hu, Z. Tian, J. Gu, T. Zhang, F. Yang, M. Ouyang, Experimental and modeling study on energy flow of 250 kW alkaline water electrolysis system under steady state conditions and cold start process, *Fuel* 350 (2023) 128799.
- [41] G. Sakas, A. Ibáñez-Rioja, V. Ruuskanen, A. Kosonen, J. Ahola, O. Bergmann, Dynamic energy and mass balance model for an industrial alkaline water electrolyzer plant process, *Int. J. Hydrogen Energy* 47 (7) (2022) 4328–4345.
- [42] X. Qiu, H. Zhang, Y. Qiu, Y. Zhou, T. Zang, B. Zhou, R. Qi, J. Lin, J. Wang, Dynamic parameter estimation of the alkaline electrolysis system combining Bayesian inference and adaptive polynomial surrogate models, *Appl. Energy* 348 (2023) 121533.
- [43] P. Olivier, C. Bourasseau, P. B. Bouamama, Low-temperature electrolysis system modelling: A review, *Renew. Sustainable Energy Rev.* 78 (2017) 280–300.
- [44] C. Daoudi, T. Bounahmidi, Overview of alkaline water electrolysis modeling, *Int. J. Hydrogen Energy* 49 (2024) 646–667.
- [45] O. A. Aguirre, C. Ocampo-Martinez, O. Camacho, Control strategies for alkaline water electrolyzers: A survey, *Int. J. Hydrogen Energy* 86 (2024) 1195–1213.
- [46] Y. Qiu, H. Zhang, Y. Zhou, T. Zang, B. Zhou, G. Chen, Nonlinear model predictive control of alkaline electrolyzers to provide ancillary services, in: *2024 IEEE 7th Int. Electrical Energy Conf. (CIEEC)*, IEEE, 2024, pp. 2819–2824.
- [47] X. Li, D. Gao, J. Tang, R. Lin, H. Li, R. Qi, L. Sha, C. Yang, W. Li, Optimization of chemical engineering control for large-scale alkaline electrolysis systems based on renewable energy sources, *Int. J. Hydrogen Energy* 93 (2024) 193–206.
- [48] Y. Zheng, S. You, H. W. Bindner, M. Münster, Optimal day-ahead dispatch of an alkaline electrolyser system concerning thermal–electric properties and state-transitional dynamics, *Appl. Energy* (2022) 118091.
- [49] G. Zhang, X. Wan, A wind-hydrogen energy storage system model for massive wind energy curtailment, *Int. J. Hydrogen Energy* 39 (3) (2014) 1243–1252.
- [50] J. Wang, J. Wen, J. Wang, B. Yang, L. Jiang, Water electrolyzer operation scheduling for green hydrogen production: A review, *Renew. Sustainable Energy Rev.* 203 (2024) 114779.
- [51] C. Varela, M. Mostafa, E. Zondervan, Modeling alkaline water electrolysis for power-to-x applications: A scheduling approach, *Int. J. Hydrogen Energy* 46 (14) (2021) 9303–9313.
- [52] Y. Qiu, B. Zhou, T. Zang, Y. Zhou, S. Chen, R. Qi, J. Li, J. Lin, Extended load flexibility of utility-scale P2H plants: Optimal production scheduling considering dynamic thermal and HTO impurity effects, *Renew. Energy* 217 (2023) 119198.
- [53] J. Li, B. Yang, J. Lin, F. Liu, Y. Qiu, Y. Xu, R. Qi, Y. Song, Two-layer energy management strategy for grid-integrated multi-stack power-to-hydrogen station, *Applied Energy* 367 (2024) 123413.
- [54] Y. Qiu, Y. Zhou, S. Chen, T. Zang, B. Zhou, Flexibility assessment and aggregation of alkaline electrolyzers considering dynamic process constraints for energy management of renewable power-to-hydrogen systems, *Renew. Energy* 235 (2024) 121261.
- [55] X. Cheng, J. Lin, F. Liu, Y. Qiu, Y. Song, J. Li, S. Wu, A coordinated frequency regulation and bidding method for wind-electrolysis joint systems participating within ancillary services markets, *IEEE Trans. Sustainable Energy* 14 (3) (2023) 1370–1384.
- [56] A. Guan, S. Zhou, W. Gu, Z. Wu, X. Ai, J. Fang, Frequency response coefficient optimal allocation strategy for multi-stacks alkaline water electrolyzer plant, *Int. J. Hydrogen Energy* 89 (2024) 151–160.
- [57] Y. Zeng, Y. Qiu, J. Zhu, S. Chen, B. Zhou, J. Li, B. Yang, J. Lin, Scheduling multiple industrial electrolyzers in renewable P2H systems: A coordinated active-reactive power management method, *IEEE Trans. Sustainable Energy* 16 (1) (2024) 201–214.
- [58] P. Diéguez, A. Ursúa, P. Sanchis, C. Sopena, E. Guelbenzu, L. Gandía, Thermal performance of a commercial alkaline water electrolyzer: Experimental study and mathematical modeling, *Int. J. Hydrogen Energy* 33 (24) (2008) 7338–7354.
- [59] P. Trinke, P. Haug, J. Brauns, B. Bensmann, R. Hanke-Rauschenbach, T. Turek, Hydrogen crossover in pem and alkaline

- water electrolysis: mechanisms, direct comparison and mitigation strategies, *J. Electrochem. Soc.* 165 (7) (2018) F502.
- [60] M. Baldea, I. Harjunkoski, Integrated production scheduling and process control: A systematic review, *Comput. Chem. Eng.* 71 (2014) 377–390.
- [61] Y. Qiu, J. Lin, F. Liu, N. Dai, Y. Song, Continuous random process modeling of agc signals based on stochastic differential equations, *IEEE Trans. Power Syst.* 36 (5) (2021) 4575–4587.
- [62] Y. Qiu, J. Lin, F. Liu, Y. Song, G. Chen, L. Ding, Stochastic online generation control of cascaded run-of-the-river hydropower for mitigating solar power volatility, *IEEE Trans. Power Syst.* 35 (6) (2020) 4709–4722.
- [63] C. N. Jones, M. Morari, Polytopic approximation of explicit model predictive controllers, *IEEE Trans. Automat. Control* 55 (11) (2010) 2542–2553.
- [64] A. Bemporad, M. Morari, Control of systems integrating logic, dynamics, and constraints, *Automatica* 35 (3) (1999) 407–427.